Rare Metals

WILEY | 有科出版 YOUKE PUBLISHING

REVIEW OPEN ACCESS

MXene-Based Electromagnetic Attenuation Materials in Microwave and Terahertz Bands

Guozheng Zhang[1] | Sitong Li[1] | Libo Chang[1] | Zelin Zhao[1] | Tianze Zhang[1] | Si Chen[1] | Xuehang Wang[2] | Zhe Wu[1] | Tianpeng Ding[1] | Xu Xiao[1]

[1]State Key Laboratory of Electronic Thin Film and Integrated Devices, School of Physics, University of Electronic Science and Technology of China, Chengdu, China | [2]Department of Radiation Science and Technology, Delft University of Technology, Delft, the Netherlands

Correspondence: Xu Xiao (xuxiao@uestc.edu.cn) | Si Chen (hello.si.chen@uestc.edu.cn) | Xuehang Wang (X.wang-22@tudelft.nl) | Zhe Wu (zhewu@uestc.edu.cn) | Tianpeng Ding (dingtp@uestc.edu.cn)

Received: 30 May 2025 | **Revised:** 6 November 2025 | **Accepted:** 7 November 2025

Keywords: electromagnetic absorption | electromagnetic interference shielding | modulation | MXenes | terahertz

ABSTRACT

MXenes exhibit considerable potential for developing high-performance electromagnetic (EM) shielding and absorption materials operating across microwave and terahertz frequencies, due to their tunable surface chemistry and exceptional charge carrier transport properties. Nevertheless, a profound understanding and precise manipulation of their broadband attenuation mechanisms remain challenging. In this review, we first examine $Ti_3C_2T_x$ MXene as a representative system to explore EM attenuation mechanisms through polarization and conductive loss models across microwave and terahertz bands. We then discuss tuning strategies, including component tailoring, interlayer regulation, film architecture, and dynamic modulation, which are supported by both classic and emerging studies, and evaluate their impact on attenuation performance. Finally, we outline future research priorities and development directions for MXene-based EM attenuation materials. By synthesizing recent advances, this review aims to establish the structure–property relationships in MXenes and to provide forward-looking insights for the field.

1 | Introduction

Electromagnetic (EM) waves are of great significance to wireless communications and will continue to play an essential role in the information age. Nowadays, widely-used 5G networks have been providing diverse digital services, including immersive experiences and Internet of Things (IoT), significantly improving user experience [1]. As the next generation communication technology, 6G technology expands to the high-frequency spectrum, dramatically improves the data transmission rate, and reduces the delay, enabling breakthrough developments in, but not limited to, extended reality (XR), artificial intelligence, and telemedicine [2], and it is expected to be commercially available between 2027 and 2030 [3]. Considering differentiated services of high-speed transmission rates and widespread signal coverage, 6G technology will extensively utilize spectrum resources from several GHz to ~3 THz [4, 5], and thus create a more complex and intense EM interference (EMI) environment, demanding more effective management and controlment on EM radiation to ensure normal operation of equipment.

The development of EM absorption materials operating at microwave and terahertz frequencies has been widely recognized as one of the most promising strategies to address EM pollution in the coming 6G era [6–10]. However, significant frequency spans lead to different EM attenuation mechanisms [11, 12], posing difficulties in developing broadband-compatible EM absorption materials. For example, dipole relaxation and magnetic loss, which are the important loss mechanisms in the microwave band, usually contribute minimally to the terahertz wave attenuation [13, 14]. Conversely, the interaction between the free charges and EM wave dominates the terahertz attenuation

process [15]. Fortunately, MXenes possessing multiple coexisting attenuation mechanisms have proven to be the promising EM attenuation materials for both gigahertz and terahertz bands, attracting tremendous attention [16, 17].

MXenes, a family of two-dimensional (2D) transition metal carbides and nitrides, were initially prepared by etching the A-layer atoms from their parent MAX phases with hydrofluoric acid. The "-ene" suffix indicates their graphene-like morphology [18]. MXenes and their precursor MAX phases follow the general formula $M_{n+1}X_nT_x$ and $M_{n+1}AX_n$ (n = 1–4), respectively. Here, M denotes an early transition metal or a combination of multiple transition metals, X generally denotes carbon, nitrogen, or a combination thereof, and T_x denotes the terminations over the surface of MXenes. Typically, MXenes prepared by HCl/HF etching contain -F, -Cl, -OH -O terminations [19]. A was initially used to represent the main group elements [20–22] (such as Al, Si, Ga, and In). After years of research efforts, MAX and MXene families continue to grow by expanding the number of elements and atomic layers [23–25]. To date, A-site elements have been extended to late transition metals [26] (Figure 1). MXenes exhibit adjustable EM properties due to their tunable surface and rich element combinations. These properties are conducive to fully realizing multifunctional and multi-band EM wave-absorbing materials and devices [27]. Thus, MXenes are expected to serve as a bridge connecting the microwave and terahertz bands, showing attractive application prospects.

Although microwave attenuation mechanisms have been explored in the past decades, and a series of superior microwave attenuation materials have come to the fore [28–30], terahertz attenuation is still in its infancy, which poses an obstacle to broadband-compatible EM pollution elimination. As a kind of material featuring multiple attenuation mechanisms in both microwave and terahertz bands, MXenes are of great potential in next-generation communication technologies; thus, a systematic review is urgently needed. In this review, we discuss the EM attenuation mechanisms of $Ti_3C_2T_x$ MXene in microwave and terahertz bands according to the Debye relaxation theory and the Drude–Smith model, respectively. Subsequently, we introduce strategies for tuning the attenuation characteristics of MXenes in microwave and terahertz bands, including composition tailoring and dynamic modulation. Finally, we present the main challenges that need to be addressed in the development of MXene-based EM attenuation materials.

2 | EM Attenuation Characteristics of $Ti_3C_2T_x$

The evolving demands of 6G technologies impose critical requirements on EM attenuation materials, necessitating fundamental understanding of their loss mechanisms across both microwave and terahertz spectral regimes. Although the microwave band (2–18 GHz) has been extensively studied for practical applications [15], there remains a critical knowledge gap in developing physics-based models to elucidate the attenuation characteristics. In contrast, the terahertz spectrum (0.1–10 THz), serving as a technological bridge between electronics and photonics, remains in the nascent stage of exploration [31]. Given its exceptional attenuation performance and research prominence, this chapter employs $Ti_3C_2T_x$ MXene as an example to systematically investigate EM attenuation mechanisms across both microwave and terahertz bands through theoretical modeling. Subsequent chapters will demonstrate the regulation of EM loss properties in MXenes through compositional engineering and dynamic modulation strategies.

2.1 | EM Attenuation Models and Mechanisms

The interaction of EM waves with materials leads to transmission, reflection, and absorption phenomena. The EM attenuation properties govern a material's impedance, which fundamentally determines these distinct behaviors. For instance, materials exhibiting strong attenuation rapidly dissipate incident waves through absorption, resulting in substantially diminished transmission signals. However, impedance mismatch induces intense reflection at the interface, markedly reducing the intensity of the incoming wave. Consequently, such materials typically exhibit low absorption efficiency and are commonly utilized in EM interference shielding applications. On the contrary, appropriately reducing the attenuation properties can improve impedance matching. Although this results in less intense dissipation of the incident wave, it suppresses reflection and enhances both wave penetration and absorption efficiency. For example, MXene-matrix composites can be engineered with tailored attenuation properties to achieve highly efficient EM absorption [32, 33]. Furthermore, variations in attenuation behavior are quantitatively captured through intrinsic EM parameters, predicting EM-matter interactions. Nevertheless, the strong frequency dependence exhibited by these EM parameters complicates the rational design of broadband devices, including wideband absorbers. In this section, we elucidate the frequency-dependent EM properties through mechanistic analysis and theoretical modeling to facilitate a deeper understanding of loss mechanisms in MXenes.

2.1.1 | EM Attenuation Model

The coexistence of multiband attenuation mechanisms necessitates a systematic analysis of loss models to understand the frequency-dependent dissipation pathways of MXenes. Here we dissect the EM attenuation framework into fundamental components, identifying four critical attenuation components associated with MXenes (Figure 2). The EM parameters can be alternatively parameterized using the following conventions: complex relative permittivity ($\tilde{\varepsilon}(\omega) = \varepsilon'(\omega) + i\varepsilon''(\omega)$) and complex conductivity ($\tilde{\sigma}(\omega) = \sigma'(\omega) + i\sigma''(\omega)$). Here, ε' quantifies capacitive energy storage, whereas ε'' governs dielectric loss. Analogously, σ' corresponds to ohmic dissipation, and σ'' reflects phase retardation. The intrinsic relationship between these parameters is given as follows:

$$\tilde{\sigma}(\omega) = -i\omega\varepsilon_0(\tilde{\varepsilon}(\omega) - \varepsilon_\infty) \quad (1)$$

where ε_∞ denotes the high-frequency permittivity dominated by electronic displacement polarization. For analytical clarity in

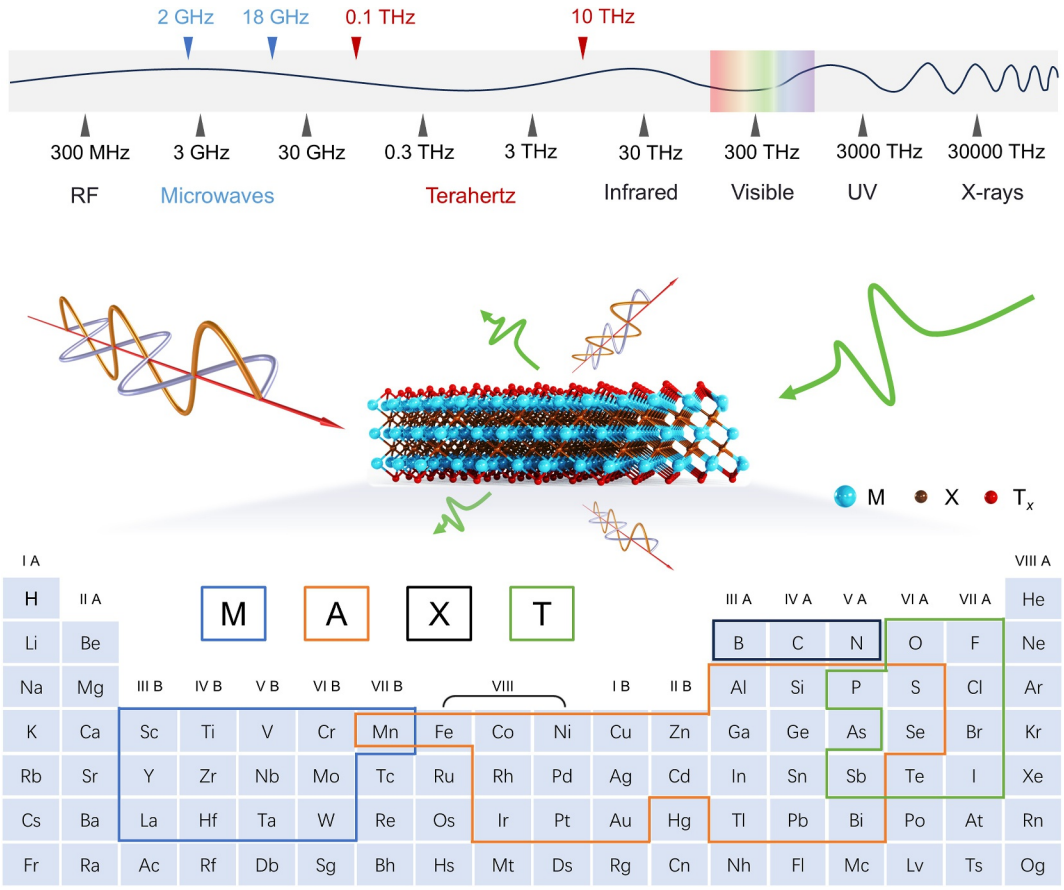

FIGURE 1 | Schematic illustration of EM spectrum and EM waves interacting with MXene. A periodic table shows elements involved in forming MAX phases and MXenes.

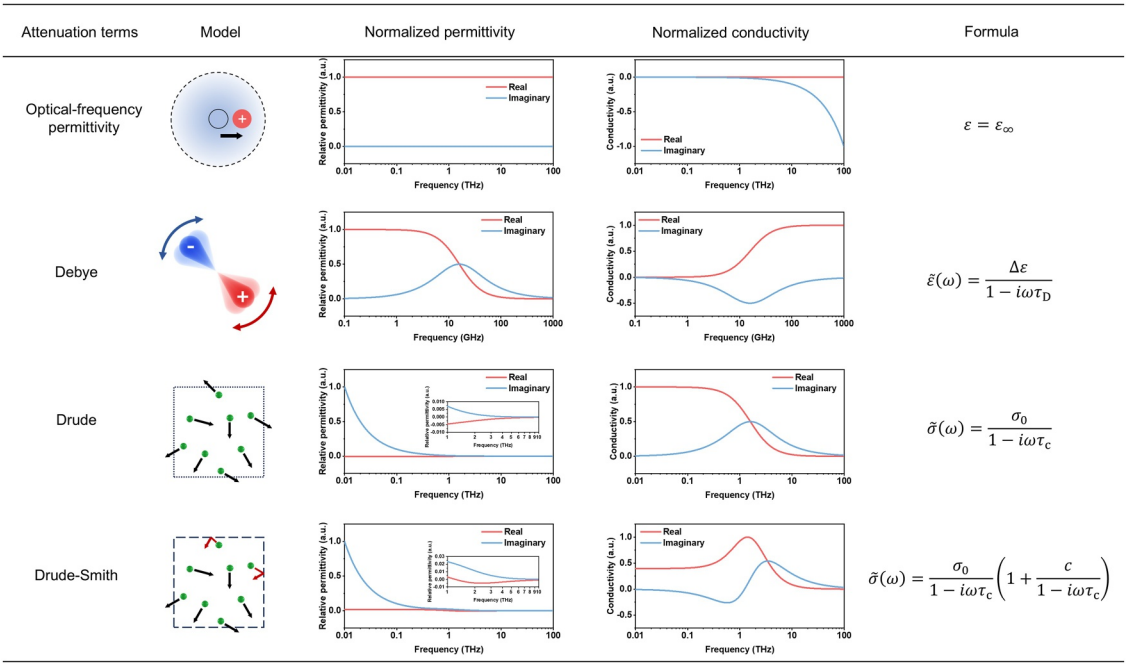

FIGURE 2 | EM attenuation models for MXenes in microwave and terahertz band.

isolating loss mechanisms, we temporarily disregard ε_∞, reducing the expression to the following equation:

$$\tilde{\sigma}(\omega) = -i\omega\varepsilon_0\tilde{\varepsilon}(\omega) \tag{2}$$

The optical-frequency permittivity (ε_∞) fundamentally originates from electronic displacement polarization, where femtosecond-scale electron cloud distortion governs the high-frequency dielectric response. In the microwave and terahertz bands, ε_∞ is characterized by a frequency-independent real permittivity (ε') existing concurrently with an imaginary part (ε'') that approaches zero, indicating negligible dielectric loss. Despite this, ε' critically regulates wave impedance matching and contributes to dispersion characteristics, affecting the incidence and interference of broadband EM waves.

The Debye relaxation process manifests pronounced frequency dispersion in ε' near the characteristic relaxation frequency, accompanied by a distinctive dielectric loss peak when plotted in logarithmic frequency coordinates. Each Debye relaxation process can be expressed as follows:

$$\tilde{\varepsilon}(\omega) = \frac{\Delta\varepsilon}{1 - i\omega\tau_D} \tag{3}$$

where $\Delta\varepsilon_j$ is the permittivity difference during the relaxation process, related to the polarization intensity, $\omega = 2\pi f$ is the angular frequency, and τ_D is the Debye relaxation time. The rapid decrease of ε' facilitates broadband destructive interference at a specific thin thickness, thereby promoting broadband absorption. In this regard, appropriate $\Delta\varepsilon$ and τ_D are necessary to construct an optimized dielectric profile [34]. Specifically, for nonferromagnetic metal-backed absorbers with a subwavelength thickness, broadening the absorption bandwidth around the target frequency generally requires meeting at least two conditions: the central frequency should be close to $\frac{1}{2\pi\tau_D}$, and ε' should approximate $\left(\frac{c_0}{4df}\right)^2$ over a broad frequency range, where c_0 is the speed of light in vacuum, and d represents the thickness of the absorber. However, excessive contributions from ε_∞ suppress dispersion strength, limiting subwavelength absorber bandwidth.

The Drude model describes the carrier transport characteristics based on isotropic relaxation (scattering), thus presenting a conductivity profiles analogous to permittivity in Debye model. The frequency-dependent conductivity is given follows:

$$\tilde{\sigma}(\omega) = \frac{\sigma_0}{1 - i\omega\tau_c} \tag{4}$$

where τ_c is the carrier relaxation time, and σ_0 is the static conductivity for isotropic scattering, which has two forms of expression [35]:

$$\sigma_0 = \frac{Nq^2\tau_c}{m^*} = \varepsilon_0\omega_p^2\tau_c \tag{5}$$

where N is the charge carrier density, q is the elementary charge, m^* is the carrier effective mass. ω_p is the plasma frequency, and ε_0 is the permittivity of vacuum.

The Drude–Smith model is an extension of the Drude model and describes the behavior in weakly confined systems where long-distance carrier transport is hindered. In the Drude–Smith model, carrier scattering is considered anisotropic, and the backscattering coefficient c is introduced in the formula [36, 37]. The complex conductivity $\tilde{\sigma}(\omega)$ can be expressed as follows:

$$\tilde{\sigma}(\omega) = \frac{\sigma_0}{1 - i\omega\tau_c}\left(1 + \frac{c}{1 - i\omega\tau_c}\right) \tag{6}$$

where c ranges from -1 to 0. When $c = -1$, the carriers are considered to be completely backscattered. If $c = 0$, this formula can be simplified to the Drude model.

EM parameters, derived from modeling or experimental measurements, enable the evaluation of key attenuation-related performance metrics: EM interference (EMI) shielding effectiveness (SE) [38], thin films intrinsic absorption [15], reflection loss (RL), and effective absorption bandwidth (EAB) [39]. Furthermore, EMI SE comprises three distinct components defined by their attenuation mechanisms: SE_T (total SE, quantified via transmittance), SE_R (SE attributed to reflections), and SE_A (absorptive SE arising from EM dissipation within the medium).

2.1.2 | Microwave Attenuation Mechanism

The microwave attenuation in materials arises from a synergistic interplay between dielectric loss and magnetic loss. Dielectric loss can be further categorized into polarization relaxation loss and conductive loss.

Polarization relaxation occurs among bound charges, where separation and rearrangement of positive and negative charges under alternating EM fields lead to significant energy dissipation within specific frequency ranges. At sufficiently high frequencies, the reversal of charges can no longer keep pace with the electric field oscillation, resulting in diminished dielectric loss. This process is generally described by Debye relaxation theory. Depending on the polarization type, polarization relaxation primarily arises from interface polarization (Maxwell–Wagner–Sillars mechanism) [40] and dipole polarization [41]. Interfacial polarization originates from the collective accumulation of charges within heterojunctions [42], whereas dipole polarization results from localized charge separation at defects, dopant atoms, or functional groups. These polarization sites undergo relaxation loss during reorientation under an alternating electric field. Through rational design of polarization sources, both $\Delta\varepsilon$ and τ_D can be effectively modulated, enabling the potential construction of a broad absorption bandwidth. However, due to its relatively long relaxation time, polarization relaxation is relatively weak within the terahertz band.

Conductive loss originates from electron–phonon interactions during charge carrier transport, through which EM energy is dissipated as heat [43, 44]. Owing to the short relaxation time of carriers (several to several hundred femtoseconds), electrical conductivity in the microwave band exhibits negligible dispersion

and remains effectively equivalent to the DC conductivity [15]. Within the dielectric spectrum, conductive loss contributes predominantly to the imaginary part of the permittivity, which decreases significantly with increasing frequency, while exerting minimal influence on the real part. Appropriate conductive loss can facilitate impedance matching, whereas excessive conductive loss leads to strong reflection. Furthermore, because conductive loss contributes relatively little to the real part of permittivity in the microwave band, it is unfavorable for generating a dispersive dielectric profile capable of supporting broadband destructive interference. Hence, in metal-backed structure absorbers, materials dominated by conductive loss generally cannot reach broadband absorption. In practical applications across the microwave band, this behavior is commonly modeled using either the Drude or Drude–Smith model, where a carrier relaxation time approaching zero is assumed for analytical simplicity.

Magnetic loss serves as a vital loss path in microwave. The magnetic loss in the microwave band is mainly caused by natural resonance [45], exchange resonance [46], hysteresis loss, and eddy current loss [47], each of which has been systematically elucidated in prior comprehensive studies [48, 49]. In the case of MXenes, strategies such as defect engineering [50], structural distortion [51] or compositional design [52, 53] can induce intrinsic ferromagnetism, thereby potentially enhancing EM attenuation performance. However, conventional MXenes (typically lacking Fe, Co, or Ni at the M-site) exhibit limited atomic magnetic moments and low saturation magnetization, resulting in negligible magnetic loss contributions. Consequently, the magnetic loss in MXene-based systems currently depends heavily on the intrinsic properties of integrated magnetic components [54].

2.1.3 | Terahertz Wave Attenuation Mechanism

Terahertz attenuation is strongly influenced by conductive loss. In contrast to the microwave band, terahertz conductivity exhibits pronounced dispersion due to the comparable timescales of the wave frequency and the carrier relaxation frequency. This frequency-dependent behavior concurrently influences both the real and imaginary parts of the permittivity. Energy dissipation during free carrier transport occurs primarily due to scattering from ionic cores, whereby momentum and energy are transferred to the lattice. This mechanism is well described by the Drude model. However, in weakly confined systems such as nanomaterials [55, 56], disordered crystals [57, 58], molecular networks [45, 59], and under high field transport conditions, low frequency conductivity becomes suppressed and deviates from the Drude model. To address these anomalies, the Drude–Smith model has been developed as an extension. It incorporates a "carrier backscattering" mechanism, also referred to as a memory effect, offering a more accurate description of carrier dynamics in weakly confined systems, including the terahertz conductive response of MXene films [60].

In the terahertz band, for metal-backed structure absorbers under a subwavelength thickness, even if the material is mainly governed by conductive loss, it is possible to engineer the permittivity through precise modulation of conductivity parameters, thereby enabling high-efficiency broadband absorption. For supported-film absorbers with a thickness negligible compared to the wavelength, low-dispersion conductivity enables broadband absorption, which necessitates a low carrier relaxation time. Optimizing parameters such as σ_0, τ_c, c, and d allows simultaneous impedance matching and attainment of the intrinsic absorption limit of 50%.

Beyond EM attenuation caused by conductive losses, the terahertz spectral range encompasses a variety of elementary excitations that exhibit resonant responses at specific frequencies. These excitations include molecular rotations [61], vibrational modes [62], low-lying electronic transitions [63–65], etc., as documented in previous studies. Such resonances enable strong narrowband EM–matter interactions and can be effectively modeled using a Lorentz oscillator model. However, the Lorentz model typically exhibits narrow-band interactions with EM waves and will not be discussed in detail here.

Moreover, we specifically address the potential for achieving compatible broadband absorption across both microwave and terahertz frequencies using a uniform metal-backed planar absorber structure. The requirement for the dominant loss mechanism presents an inherent challenge: microwave absorption favors a secondary role for conductive loss, whereas terahertz absorption requires its dominance. This dichotomy appears contradictory for achieving broadband performance. Nevertheless, advanced microwave absorbers satisfying impedance-matching conditions are typically fabricated at millimeter-scale thicknesses—far greater than the wavelengths of terahertz waves. This large thickness allows strong EM attenuation even when the imaginary part of the permittivity remains modest. Moreover, filler-matrix composite structures, which often exhibit high backscattering coefficients describable by the Drude–Smith model, provide additional enhancement to terahertz conductivity. Therefore, by tuning polarization and conductive losses to dominate microwave and terahertz absorption, respectively, it is possible to realize high-efficiency broadband absorbers.

2.2 | Microwave Attenuation Characteristics of $Ti_3C_2T_x$

The tunable electrical conductivity and chemically diverse surface functional groups of MXenes create a synergistic interplay that enables broadband EM wave-matter interactions across microwave to terahertz frequencies. Since its discovery, $Ti_3C_2T_x$ MXene has attracted extensive research interest owing to its exceptional electrical conductivity within the MXene family [66]. A landmark study by Gogotsi's group in 2016 demonstrated that solution-processed MXene films of varying thicknesses achieved unprecedented EM shielding performance, with a 45 μm-thick $Ti_3C_2T_x$ film exhibiting an outstanding SE_T of 92 dB in the X-band (Figure 3A,B) [6]. It should be noted that the measurements of shielding effectiveness SE_T are performed in waveguides, where geometric confinement effects (e.g., TE_{10} mode propagation in rectangular waveguides) inherently modify EM boundary conditions compared to free-space scenarios. To resolve this discrepancy and demonstrate planar-wave shielding

characteristics, we employed transfer matrix modeling (TMM) to reconstruct the SE_T performance of 11.2-μm MXene films under free-space (Figure 3C) [70]. The reconstructed SE_T still maintains high performance and improves with increasing frequency. While high electrical conductivity remains the primary determinant of EMI SE [71], $Ti_3C_2T_x$ MXene exhibits comparable SE_T values to conventional metals like copper and aluminum, despite possessing electrical conductivity two orders of magnitude lower [72]. This remarkable performance has been attributed to synergistic shielding mechanisms involving multiple internal reflections and dipole polarization relaxation losses, which collectively enhance EM wave attenuation capabilities, enabling simultaneous enhancement of interfacial reflection and rapid absorption of incident EM energy, thereby improving the SE_T. However, the fundamental EM attenuation mechanisms in MXenes remain insufficiently understood, particularly regarding the relative contributions of various energy dissipation pathways. These seminal findings have catalyzed burgeoning interest in deciphering the EM attenuation characteristics of MXene-based materials, establishing a new research frontier in advanced EM attenuation development.

The ultra-high EMI shielding behavior of $Ti_3C_2T_x$ has generated siginificant interest among researchers. In order to analyze the possible existence of conductive loss and multiple polarization relaxation loss, the Drude–Smith–Debye (DSD) equation is introduced here, expressed as follows:

$$\tilde{\varepsilon}(\omega) = \varepsilon_\infty + \sum_j \frac{\Delta\varepsilon_j}{1 - i\omega\tau_D} + \frac{i\sigma_0}{\omega\varepsilon_0(1 - i\omega\tau_c)}\left(1 + \frac{c}{1 - i\omega\tau_c}\right) \quad (7)$$

The exceptionally short electron relaxation time (τ_c) at femtosecond scale results in $\omega\tau_c$ approaching 0 within the microwave frequency range. Through complex permittivity decomposition,

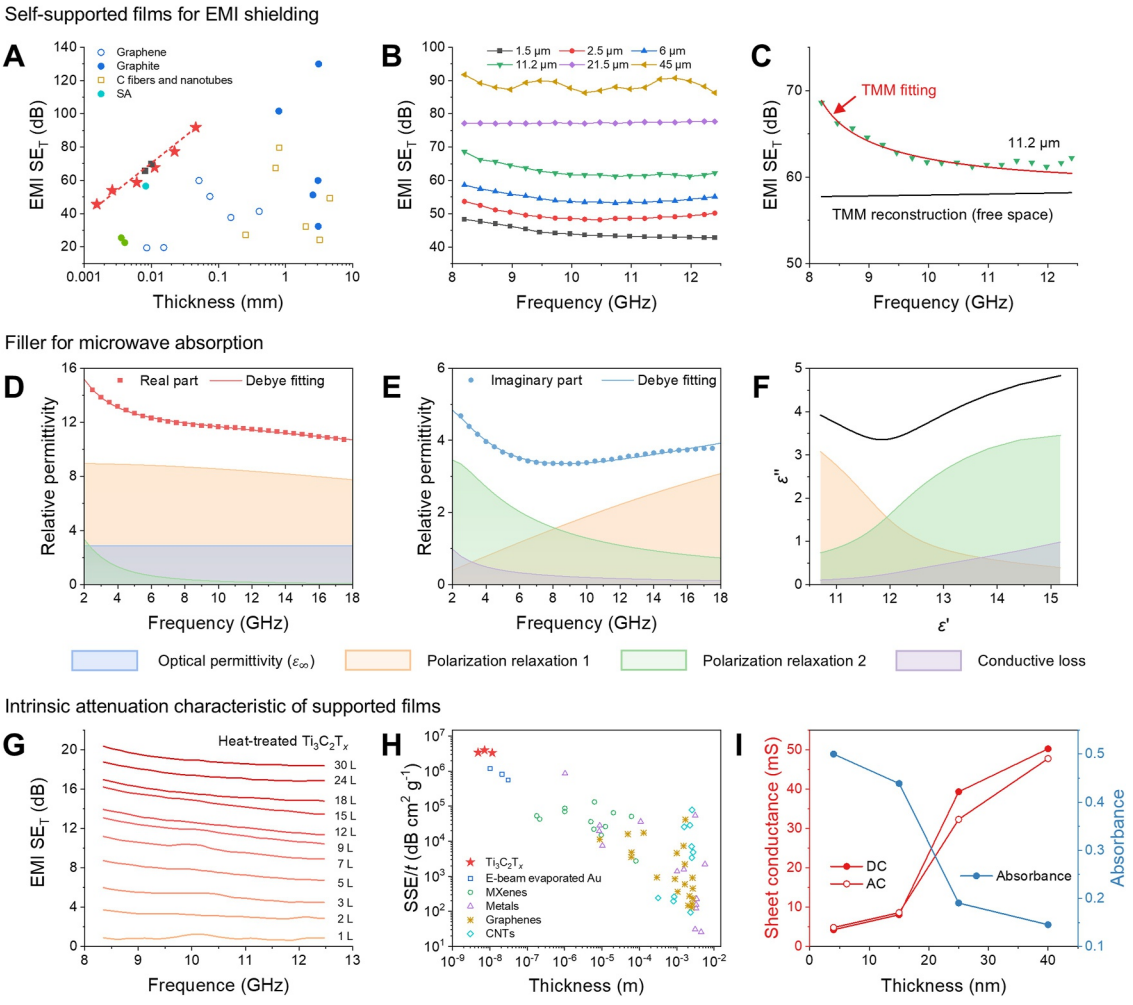

FIGURE 3 | Microwave attenuation properties of $Ti_3C_2T_x$ MXene. (A) EMI SE_T versus thickness of different materials. (B) EMI SE_T versus frequency for $Ti_3C_2T_x$ films under different thicknesses. (C) EMI SE_T for $Ti_3C_2T_x$ film at a thickness of 11.2 μm and the corresponding SE_T reconstructed in the free space. Reproduced with permission from Ref. [6]. Copyright 2016, American Association for the Advancement of Science. (D) Real part of relative permittivity, (E) imaginary part of relative permittivity, and (F) cole-cole plot for multi-layered $Ti_3C_2T_x$/paraffin composite with a loading ratio of 40 wt% and the contribution of attenuation terms fitted by the DSD equation. Reproduced with permission from Ref. [67]. Copyright 2020, Elsevier. (G) EMI SE_T verse frequency of heat-treated $Ti_3C_2T_x$ films with various layers. (H) SSE/t verse thickness of $Ti_3C_2T_x$ and other electrically conductive films. Reproduced with permission from Ref. [68]. Copyright 2020, Wiley-VCH. (I) Absorbance and sheet conductance verse thickness of spray-coated $Ti_3C_2T_x$ films. Reproduced with permission from Ref. [69]. Copyright 2023, AIP Publishing.

the DSD equation can be simplified to the classical modified Debye equation is expressed as follows [73]:

$$\varepsilon'(\omega) = \varepsilon_\infty + \sum_j \frac{\Delta\varepsilon_j}{1+\omega^2\tau_{Dj}^2} \tag{8}$$

$$\varepsilon''(\omega) = \sum_j \frac{\Delta\varepsilon_j}{1+\omega^2\tau_{Dj}^2}\omega\tau_D + \frac{\sigma_{DC}}{\omega\varepsilon_0} = \sum_j \varepsilon_p''(\omega) + \varepsilon_c''(\omega) \tag{9}$$

where ε_p'' is attributed to polarization loss, while ε_c'' ($\varepsilon_c'' = \frac{\sigma_{DC}}{\omega\varepsilon_0}$) is attributed to conductive loss, $\sigma_{DC} = \sigma_0(1 + c)$ represents the DC conductivity.

According to the modified Debye equation, we systematically analyzed the microwave attenuation characteristics of multilayer $Ti_3C_2T_x$/paraffin composite (with 40 wt% loading ratio) [67]. The paraffin serves as a molding matrix with minimal dielectric loss, effectively suppressing parasitic absorption from the composite matrix. However, its optical-frequency permittivity ($\varepsilon_\infty \approx 2.3$) weakened the dispersion characteristics of ε'. Figure 3D,E shows the real and imaginary parts of the complex relative permittivity, respectively, revealing multiple relaxation characteristics. Due to the limited range of the measurement spectrum, only two relaxation terms were employed for fitting. The fitted ε_∞, $\Delta\varepsilon_1$, τ_{D1}, $\Delta\varepsilon_2$, τ_{D2}, σ_{DC} are 2.87, 6.91, 82.1 ps, 8.97, 3.51 ps, 0.11 S m^{-1}, respectively. Figure 3F shows the Cole–– x-axis, but due to the contribution of conductive loss, the centers of the two arcs deviate from the x-axis [74]. In summary, multilayered $Ti_3C_2T_x$/paraffin with a loading ratio of 40 wt% has an EAB of 4 GHz (14–18 GHz) at 1.5 mm. When used as fillers, multilayer MXenes exhibit moderate performance due to the cancellation of macroscopic dipole moments and the lack of a conductive network [67, 75–77]. However, fully delaminated MXene can achieve impedance matching at a filling ratio of ≤ 2.1 wt% [78] in the X-band, demonstrating the great potential of low-dimensional conductive materials as lightweight absorbing fillers. However, measurement deviations persist in studies on few-layer MXene/matrix composites based on the coaxial transmission method. The previously reported dielectric constants contain undesirable Lorentz terms, indicating that intense resonance interferes with the extraction of the permittivity, potentially due to the uneven distribution of fillers or the air gap between the coaxial line and the sample [77, 79].

In addition, the distribution and stacking mode of MXene nanosheets in the composite will have a significantly impact on their conductive loss due to the substantial difference between band-like transport and hopping transport [80]. Moreover, an increase in loading ratio elevates the rotational friction coefficient of dipoles, prolonging the relaxation time [81, 82]. In contrast, the continuous MXene films possess excellent long-range conductive networks, potentially resulting in different EM attenuation properties. Therefore, the microwave attenuation characteristics of MXene fillers and films must be discussed separately to inform the design of EM attenuation materials for different application scenarios. In this regard, MXene films with uniform and controllable thickness provide ideal samples for investigation.

Yun et al. [68] prepared $Ti_3C_2T_x$ films with a controllable number of layers through self-assembly at the air-liquid interface and studied their EM shielding properties in the X-band. Due to the high electrical conductivity, a monolayer $Ti_3C_2T_x$ MXene assembly can provide a specific SE_T (1 dB, ~20% power attenuation). The SE_T increases as the thickness increases and reaches an average value of 10 dB (90% power attenuation) in the X-band for the 9-layer film. Despite the high EMI SE_T at such a thin thickness, the conductivity of $Ti_3C_2T_x$ can be further increased by removing interlayer species. A 24-layer $Ti_3C_2T_x$ film annealed at 400°C with a thickness of ~55 nm demonstrates an average EMI SE_T of 20 dB (Figure 3G). By comprehensively considering the thickness and weight, the absolute shielding effectiveness (SSE/t) values can be further calculated to comprehensively evaluate the EM shielding material (Figure 3H). Remarkably, the 3-layer $Ti_3C_2T_x$ film has a high SSE/t value of 2.83×10^6 dB cm^2 g^{-1}, which further increases to 3.89×10^6 dB cm^2 g^{-1} after annealing and demonstrates the maximum SSE/t value at the time of reporting. These results confirm that $Ti_3C_2T_x$ has excellent potential to become an efficient, light and thin EM shielding material.

Under a thin thickness, absorption is expected to dominate the EM attenuation. Obtaining substrate-independent intrinsic attenuation characteristics is beneficial in guiding the EM absorption design of MXenes on different substrates, which has attracted more attention. Recent advancements in two-dimensional transition metal carbide research have unveiled the intrinsic EM attenuation characteristics of $Ti_3C_2T_x$ MXene thin films in the X-band. Through systematic theoretical modeling, Rakhmanov et al. [69] extracted the characteristic impedance of $Ti_3C_2T_x$ films spanning thicknesses from 4 to 40 nm, revealing intrinsic absorption characteristics. Notably, ultrathin $Ti_3C_2T_x$ film (4 nm thickness) with a sheet conductance of ~4.76 mS demonstrated approximately ~50% absorption in X-band (Figure 3I), approaching the thin film intrinsic absorption limit [15]. Because 2D-layered materials have no dangling bonds, $Ti_3C_2T_x$ films offer brighter application prospects than traditional metal films, such as gold film (reaching the intrinsic absorption limit at 5 nm) [83]. For all the samples, the DC conductance and AC conductance are nearly identical, indicating that microwave-frequency EM fields induce minimal perturbation to the carrier transport mechanisms in $Ti_3C_2T_x$ films [84], thereby verifying the feasibility of using DC conductance to evaluate microwave absorption performance. In summary, $Ti_3C_2T_x$ has excellent application prospects in the microwave band due to the absence of surface dangling bonds, outstanding processing performance, and high microwave attenuation ability. Additionally, advances in designing highly conductive MXenes (e.g., $Ti_3C_{1.9}N_{0.1}T_x$) have further highlighted the remarkable EM attenuation potential of MXene family. The EM shielding performance of MXenes and other materials in the microwave frequency band is summarized in Table 1.

2.3 | Terahertz Attenuation Characteristics of $Ti_3C_2T_x$

High metallic conductivity also gives $Ti_3C_2T_x$ high terahertz wave shielding effectiveness. Choi et al. [92] investigated the terahertz wave shielding properties of MXene films on silicon

substrates. The transmitted intensity over the measured frequency range decreases with increasing film thickness, and intensity attenuation of ~10 dB was achieved with a thickness of ~500 nm (Figure 4A). In addition, they enhanced the plasmon resonance using nanoantenna structures and further enhanced the shielding effectiveness at the resonant frequency. As a detailed discussion of this topic is beyond the scope of this review, relevant literature on the metasurface absorbers can be found in subsequent studies [94–96].

In order to achieve the terahertz wave absorbing function and eliminate potential EM pollution, impedance optimization is necessary. Shui et al. [17] prepared a thin and light terahertz absorber by soaking the polyurethane (PU) sponge in $Ti_3C_2T_x$

TABLE 1 | EMI shielding properties of materials in the microwave band.

Type	Material	Electrical conductivity (S cm^{-1})	Thickness (μm)	SE (dB)	SSE/t (dB cm^2 g^{-1})	References
MXenes	Conv-$Ti_3C_2T_x$	6500	8	59	/	[70]
	HC-$Ti_3C_2T_x$	18,000	8	75		
	Ti_3CNT_x	4200	10	58		
	V_2CT_x	1400	10	49		
	Nb_2CT_x	600	10	40		
	$Mo_2Ti_2C_3T_x$	390	10	38		
	$Ti_3C_2T_x$	18,787	2	57.1	105,853	[85]
			3.8	63.1	61,762	
			5.9	69.1	43,395	
			12.2	83.9	25,279	
	$Ti_3C_{1.9}N_{0.1}T_x$	35,000	1.3	57.8	167,837	
			3.2	64.7	75,128	
			6	74.0	45,756	
			8.2	87.0	39,213	
			12.7	98.2	28,574	
			15.4	109.6	26,257	
Metal-based	Cu	/	10	82	9213	
	Al		18	78	16,049	
	Cu		10	70	7865	[70]
	Al		8	66	30,556	
	AgNW/WPU	0.035	2.3 mm	20	10,870	[86]
	PVA/Ag/$Ti_3C_2T_x$	/	145.4	101.9	36,501.5	[87]
Carbon-based	CNT mat	41.7	10.8	77	12,833	[88]
	Porous graphene	/	200	47.8	49,750	[89]
	Graphene	1136	50	62	18,300	[90]
		25,800	50	127.3	13,021	[91]
Supporting film	E-beam evaporated Au	/	10 nm		~1.19×10^6	[68]
			20 nm		~8.23×10^5	
			30 nm		~5.59×10^5	
	Heat-treated $Ti_3C_2T_x$ assemblies	~5000	2.3 nm	1.03	1.87×10^6	
			6.9 nm	6.42	3.89×10^6	
			11.5 nm	9.31	3.39×10^6	
			16.1 nm	11.89	3.09×10^6	
			20.7 nm	13.84	2.80×10^6	
			34.5 nm	14.78	1.79×10^6	
			41.4 nm	17.13	1.73×10^6	

Abbreviations: AgNW, Ag nanowire; WPU, water polyurethane.

MXene solution. The porous structure allows MXene with high EM loss capability to be dispersed within air, optimizing impedance to absorb EM waves. By adjusting the MXene loading and pore size, RL of porous MXene sponges can reach about 65 dB (Figure 4B,C).

The outstanding terahertz wave shielding and absorption characteristics have prompted researchers to investigate its intrinsic attenuation mechanisms. Li et al. [97] first studied the terahertz conductivity properties of $Ti_3C_2T_x$ thin film on a glass substrate using a terahertz time-domain spectroscopy (THz-TDS). $Ti_3C_2T_x$ films follow the Drude–Smith model with a high (~2×10^{21} cm^{-3}) intrinsic charge carrier density and relatively high (~34 cm^2 V^{-1} s^{-1}) mobility of carriers within individual nanoplatelets. A 16-nm-thick film reaches an average absorption coefficient of ~46,000 cm^{-1} in the 0.2-2 THz band, consistent with the range predicted by theory but lower than the predicted value of stacked graphene sheets. However, the terahertz attenuation characteristics of $Ti_3C_2T_x$ are not easily fully revealed in the narrow terahertz band. Zhao et al. [93] further explored the broadband absorption characteristics and terahertz wave attenuation mechanism of $Ti_3C_2T_x$ using air–plasma-biased coherent detection (ABCD) THz-TDS. The 17.2-nm-thick $Ti_3C_2T_x$ film approaches the intrinsic absorption limit (50%) in the 1–10 THz range, demonstrating the most excellent intrinsic absorption properties to date (Figure 4D,E). Improved $Ti_3C_2T_x$ film quality could further optimize this thickness to 10.2 nm. This exceptional performance originates from the short scattering time (< ~15 fs) and high carrier concentration (> ~10^{21} cm^{-3}).

To elaborate prerequisites for broadband high-efficiency intrinsic absorption, we establish a parameter mapping via the Drude–Smith model. Using a fixed film thickness of 20 nm and backscattering coefficient $c = -0.58$, we delineated critical parameter constraints (Figure 4F). According to the map, when $\omega\tau > 1$, conductivity experiences a significant decline. This phenomenon typically occurs in the terahertz frequency range due to carrier scattering times generally being on the order of tens of femtoseconds. High τ values lead to a sharp conductivity reduction at higher terahertz frequencies, which leads to different requirements for intrinsic absorption at varying ratio of

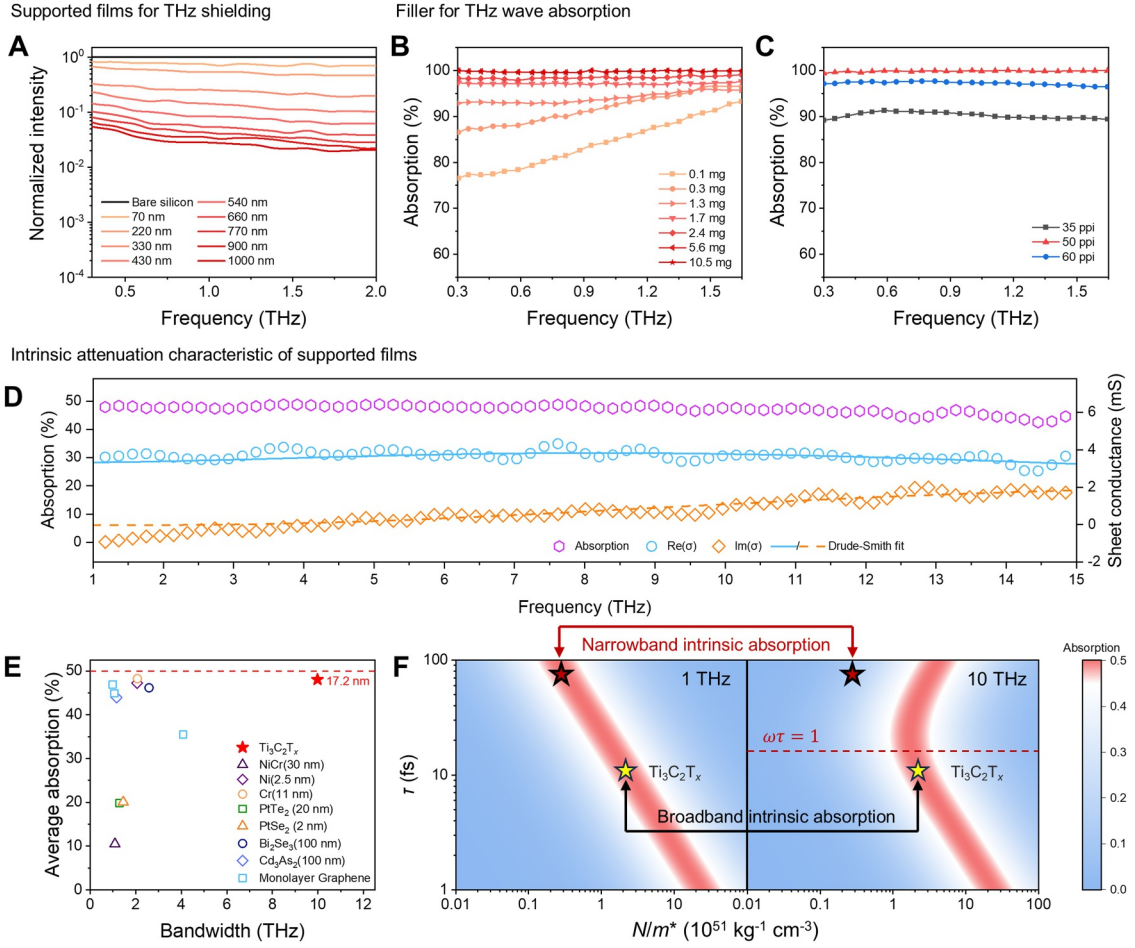

FIGURE 4 | Terahertz attenuation properties of $Ti_3C_2T_x$ MXene. (A) Normalized transmitted intensity spectra of the bare silicon and various thicknesses of MXene films on the silicon substrate. Reproduced with permission from Ref. [92]. Copyright 2018, Wiley-VCH. (B,C) THz absorption by MXene/PU sponge with different parameters. Panel (B) is with different $Ti_3C_2T_x$ loading but fixed 2 mm thickness and pore size of 50 ppi. Panel (C) is with different pore sizes but fixed 2 mm thickness and 2.8 ± 0.5 mg $Ti_3C_2T_x$ loading. Reproduced with permission from Ref. [17]. Copyright 2020, Wiley-VCH. (D) The terahertz absorbance and sheet conductance verse frequency of a 17.2-nm-thick $Ti_3C_2T_x$ film. (E) Average absorbance verse bandwidth for various materials. Reproduced with permission from Ref. [93]. Copyright 2023, Springer Nature. (F) Intrinsic absorption mapping for a 20-nm-thick film (here $c = -0.58$) at 1 and 10 THz.

carrier concentration to effective mass ($N\,m^{*-1}$) across different frequencies, thereby resulting in narrowband absorption characteristics. As scattering time decreases, the dispersion properties of sheet conductivity also diminish, which is a necessary condition for achieving broadband intrinsic absorption in the terahertz range. However, in order to achieve impedance matching at a lower scattering time and a small thickness, films are required to have high carrier concentrations. Ultrathin $Ti_3C_2T_x$ MXene assemblies meet the requirements of low scattering time and exhibit ultra-high carrier concentration, resulting in ultra-broadband strong absorption characteristics even at thin thicknesses. This combination constitutes an advantage unattainable with most other 2D materials. For instance, although graphene possesses a wide range of gate-tunable sheet carrier concentration to realize impedance matching, its long scattering time hinders its interaction with high-frequency terahertz waves [15, 58]. The terahertz electrical conductivity parameters (based on Drude or Drude–Smith model) of MXenes and other materials are summarized in Table 2. A short relaxation time leads to a high relaxation

TABLE 2 | Electrical conductivity parameters of materials in the terahertz band.

Type	Material	Thickness (nm)	σ_0 (S cm^{-1})	τ (fs)	f_r (THz)	c	References
MXenes	$Ti_3C_2T_x$	3.0	2.05×10^4	9.62	16.54	−0.82	[93]
		6.4	1.92×10^4	10.61	15.00	−0.79	
		8.0	1.88×10^4	10.73	14.83	−0.76	
		10.2	1.58×10^4	10.98	14.49	−0.72	
		11.8	1.92×10^4	12.60	12.63	−0.68	
		13.3	1.80×10^4	12.59	12.64	−0.66	
	$Mo_2Ti_2C_3T_x$	80	70	16	9.95	−0.941	[98]
	$Mo_2T_{i2}C_3T_x$ (annealed)	~50	110	20	7.96	−0.875	
	$Mo_2TiC_2T_x$	~1.3 μm	26	36	4.42	−0.864	
	$Mo_2TiC_2T_x$ (annealed)	/	22	31	5.13	−0.895	
Semimetals	Graphene (single crystal)	Monolayer	2.19 mS cm^{-1}	68	2.34	/	[58]
	Graphene (polycrystalline)		1.54 mS cm^{-1}	43	3.70	−0.60	
	Graphene (electrical gating)		0.5 mS cm^{-1}	44	3.61	/	[15]
			1.94 mS cm^{-1}	99	1.60	/	
	Graphene (chemical doping)		1.94 mS cm^{-1}	28	5.68	/	
			2.68 mS cm^{-1}	74	2.15	/	
			4.00 mS cm^{-1}	111	1.43	/	
	$PdTe_2$	5	1.36×10^4	34.46	4.62	−0.69	[99]
		10	1.47×10^4	16.31	9.76	−0.57	
		15	4.83×10^4	37.69	4.22	−0.73	
		20	5.68×10^4	29.91	5.32	−0.65	
	$PtSe_2$	3.3	12.12	69.15	2.30	−0.99	[100]
		5.8	603.45	58.25	2.73	−0.312	
		8.5	1894.12	36.59	4.35	−0.233	
Metals	Cu	/	/	23.72	6.71	/	[101]
	Al	/	/	23.12	6.88	/	
	Au (273 K)	/	/	30	5.3	/	[102]
	Au (77 K)	/	/	120	1.3	/	
	Cu (273 K)	/	/	27	5.9	/	
	Cu (77 K)	/	/	210	0.76	/	
Topological insulators	Bi_2Se_3 (5 K)	~128	546.88	~145	~1.1	/	[63]
	Bi_2Se_3 (300 K)	~120	992	~227	0.7	/	[103]
Semiconductors	n-Si (295 K)	200 μm	0.12	295	0.54	/	[104]
	n-GaAs (295 K)	190 μm	1–10	165	0.96	/	[105]
	WSe_2 ($n_h = 1.4 \times 10^{12}$ cm^{-2})	Monolayer	0.468 mS cm^{-1}	592	0.27	/	[106]
	WSe_2 ($n_h = 1.3 \times 10^{11}$ cm^{-2})	Monolayer	/	464	0.34	/	

frequency (f_r), ensuring dispersionless conductivity across the entire terahertz band. Meanwhile, a high carrier concentration promotes elevated σ_{DC}, enabling $Ti_3C_2T_x$ to exhibit highly efficient broadband film intrinsic absorption.

Interestingly, there is a vast difference in the assemblies between the DC impedance measured by the Hall effect and the AC impedance measured by terahertz time-domain spectroscopy. Combined with the Drude–Smith model, the incidence of a terahertz driving pulse can cause carrier oscillation, isotropic scattering, and backscattering, where backscattering occurs at defects and impurities within the flake, especially at the flake boundaries. Although terahertz pulses interact with MXene flakes and are converted into thermal energy, carriers oscillate over short-range distances, less affected by boundary backscattering effect than the long-range carrier migration caused by DC (even microwave). Therefore, the DC parameters cannot perfectly guide researchers in selecting excellent terahertz loss materials, which is in stark contrast to the microwave band. Additionally, it has been demonstrated that substrates affect carrier scattering in MXene assemblies, and this influence becomes particularly significant when the MXene films reach smaller thicknesses [107].

3 | Methods for Regulating the EM Attenuation Characteristics of MXenes

The composition and intercalation agent of MXenes determines their electron transport properties, significantly influencing their EM attenuation characteristics. For example, it is reported that the conductivity of $Ti_3C_2T_x$ film can be more than 1000 times higher than that of Nb_2CT_x film [108]. Replacing the -OH group of Ti_3C_2 with -O will cause a massive increase in the work function (from 2.02 to 5.97 eV) [109, 110]. Se-terminated Nb_2CT_x can enter a superconducting state at a low temperature [24]. Furthermore, MXenes possess tunable chemical compositions. This characteristic enables precise control over both conductive and polarization losses, thereby optimizing the desired microwave and terahertz attenuation parameters. In addition, dynamic modulation of MXenes' EM attenuation properties has recently stimulated significant interest, holding promise for enabling smart terahertz devices. This section describes the statical performance design of MXenes and the dynamic modulation of their attenuation characteristics to EM waves.

3.1 | Composition Tailoring

Conductive loss and polarization loss can be regulated by adjusting the M-, X-, and T_x-site species, thereby changing MXenes' EM shielding and absorption properties in microwave and terahertz bands. Therefore, significant changes in conductive and polarization loss can be achieved through composition tailoring.

3.1.1 | M-Site Replacement

M-site elements significantly contribute to the density of states (DOS) spectrum and are highly related to macroscopic electron transport [111]. Compositional engineering of the M-site further enables precise tailoring of the charge density map (Figure 5B), which directly modulates dipole polarization dynamics and can generate additional dipoles through charge redistribution [112, 114]. This atomic-level tunability establishes a multiscale framework for engineering EM wave attenuation mechanisms, providing a materials design strategy to achieve programmable microwave absorption through structural–electronic synergy.

M-site substitution enables balancing conductive and polarization losses, thereby enhancing microwave absorption performance. According to the theoretical research of Xia's group [34], strong dielectric dispersion is essential for broadening the EAB, requiring synergistic contributions from these loss mechanisms. Han et al. [78] prepared V-based MXene/PU composites and verified the above discussion through experiments. The EAB of the composites covers the whole X-band, showing extremely outstanding performance among nonmagnetic materials (Figure 5C). In detail, the optimal RL value of V_2CT_x/PU reaches −30 dB at the thickness of 3.3 mm with the loading ratio of 2.2 wt%, and that of $V_4C_3T_x$/PU reaches −39 dB at the thickness of 3.4 mm with the loading ratio of 2.1 wt%. The excellent performance is attributed to appropriate conductive loss and sufficient polarization loss. Specifically, weakened conductive loss allows more polarization units to be accommodated in the absorber in impedance matches, thereby enhancing polarization loss (at the expense of a slight increase in fill ratio). As a result, the dispersion of the real part of the permittivity increases, leading to enhanced broadband destructive Interference, thereby enhancing the EAB in the X-band. Furthermore, arranging M-site elements in disorder is another way to regulate EM attenuation characteristics and is beneficial to induce dipole polarization further, and adjust conductive loss. In this regard, Han et al. [115] proposed a solid solution strategy to modify the M-site elements of MXenes to tailor the electronic properties. Varying M-site composition will significantly alter the conductivity, thus affecting EMI shielding properties (Figure 5D) [108]. Xu et al. [116] further reveal that the solid solution strategy affects both polarization loss and conductive losses.

In addition, adjusting the M-site elements greatly impacts the terahertz response due to differences in electron transport characteristics. Titova's group reported the terahertz conductivity of $Ti_3C_2T_x$, $Mo_2Ti_2C_3T_x$, and $Mo_2TiC_2T_x$ [97, 98, 117]. $Ti_3C_2T_x$ films prepared from different batches exhibit apparent differences in terahertz conductivity, which may be influenced by various factors, such as quality, film thickness, and processing methods [93]. Fei et al. [113] provide a systematic report of the intrinsic terahertz properties of MXene thin films with varying M-site elements. An enhancement in the intrinsic terahertz absorption was correlated with increasing terahertz conductivity for MXenes at an approximate thickness of ~20 nm (Figure 5E). Moreover, the effective electron mass (m^*) in MXenes cannot be fully reduced to the free electron mass (m_0). Furthermore, the terahertz conductivity is governed by the ratio of the carrier concentration (n) to the effective mass (m^*). Additionally, although Ti_2CT_x exhibits a substantial discrepancy in DC conductivity compared to $Ti_3C_2T_x$, their AC conductivities converge within the terahertz band (Figure 5F).

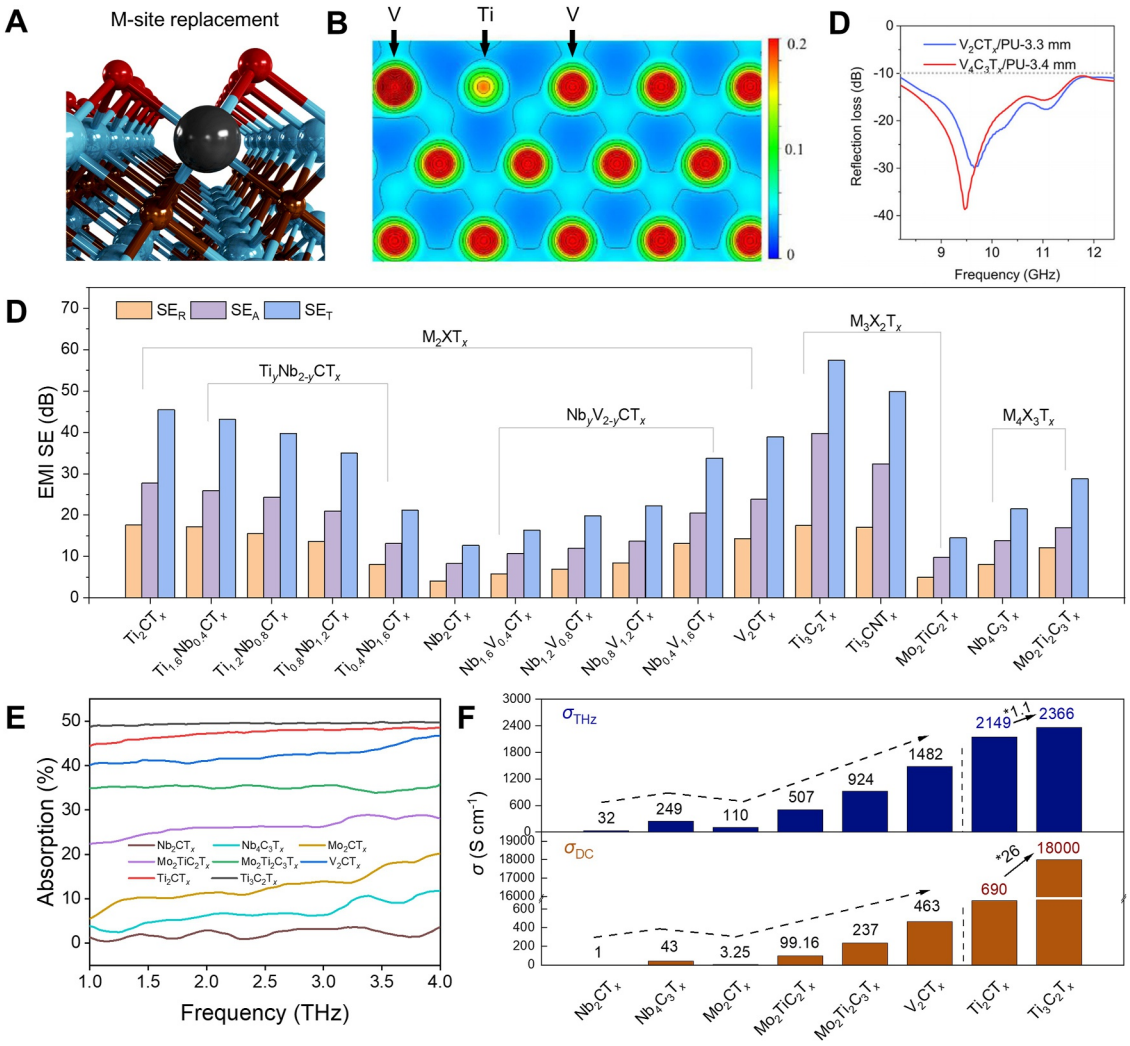

FIGURE 5 | Tuning the EM attenuation properties of MXenes via M-site substitution. (A) Schematic illustration of EM attenuation regulation through M-site replacement. (B) Charge density map of $(V_{0.8}Ti_{0.1}Cr_{0.1})_2AlC$. Reproduced with permission from Ref. [112]. Copyright 2022, Elsevier. (C) Optimal RL of V_2CT_x/PU (2.2 wt%) and $V_4C_3T_x$/PU composites (2.1 wt%). Reproduced with permission from Ref. [78]. Copyright 2022, Elsevier. (D) The average EMI SE_T of different MXene films in the X-band. Reproduced with permission from Ref. [108]. Copyright 2020, American Chemical Society. (E) Terahertz absorbance of MXene films with various M-site element. (F) Terahertz conductivity and AC conductivity of MXene films with various M-site element. Reproduced with permission from Ref. [113]. Copyright 2025, Wiley-VCH.

3.1.2 | X-Site Replacement

The X-site's critical role in governing MXene electrical transport properties, though historically overlooked, has driven substantial breakthroughs over the past 5 years. A key advancement is the progressive enhancement of electrical conductivity—imperative for boosting conductive losses and EMI SE.

In 2016, even $Ti_3C_2T_x$ synthesized via the minimally intensive layer delamination (MILD) method achieved conductivities of only 4600 S cm^{-1} [118]. By 2021, MAX precursors sintered with excess aluminum emerged as the preferred method for synthesizing select MXenes. MILD-derived $Ti_3C_2T_x$ from these precursors reached a conductivity of 20,000 S cm^{-1} (Figure 6B) [19]. Michałowski et al. [119] employed secondary ion mass spectrometry (SIMS) to demonstrate oxygen occupation in X-sites (≤ 30 at%) of conventionally sintered MAX phases and their MXene derivatives, thereby substituting carbon atoms (Figure 6C). However, excess aluminum suppresses $Ti_3AlC_{2-y}O_y$ formation. These findings align with the work by Iqbal et al. [70], which confirmed that oxygen-free X-site engineered $Ti_3C_2T_z$ delivers superior EMI SE across an ultra-broadband spectrum (110 kHz–110 GHz) than $Ti_3C_{2-y}O_yT_x$.

Theoretical insights predict that nitrogen substitution at X-sites enhances electron mobility [121], intensifying interest in nitride MXenes. Koo's group [120] reported that the 40-μm-thick Ti_3CNT_x film annealed at 350°C exhibited anomalous higher SE_T (up to 116 dB) despite their reduced conductivity relative to $Ti_3C_2T_x$ in the X-band (Figure 6D–F). However, this reason remains unexplained after considering oxidation and interlayer porosity, requiring further investigation. Recent work by Han et al. [85] demonstrates that precision engineering of nitrogen content in $Ti_3C_{2-x}N_xT_z$ enables tailored electronic transport properties. Annealed $Ti_3C_{1.9}N_{0.1}T_z$ yielded a record conductivity of 35,000 S cm^{-1} among MXenes (Figure 6G), while achieving an EMI SE_T of 87 dB with a thickness of only 8.2 μm in the X-band, surpassing 10-μm-thick copper foil and exceeding 100 dB in the

W-band (Figure 6H). This strategy marks a milestone for MXenes in EM attenuation, with significant potential for further enhancing performance. However, a further increase in nitrogen content promotes the formation of defects during etching, including voids and surface titanium vacancies, thereby reducing electrical conductivity. Consequently, the development of precise etching strategies is essential to mitigate these adverse reactions.

3.1.3 | T_x-Site Replacement

The T_x sites critically control the work function and Fermi level position [122], giving rise to unique electronic properties. For instance, theoretical calculations predict Ti_2CO_2 to be a p-type semiconductor, whereas Ti_2CF_2 and $Ti_2C(OH)_2$ exhibit metallic states [123]. Furthermore, distinct functional groups significantly alter the electron localization function value and modulate the dipole moments. These collective interactions significantly regulate EM attenuation.

Density functional theory (DFT) calculations reveal the relationship between surface terminations and the resultant dipole moments [112]. The electron localization function (ELF) plots show that electrons will be localized around -O, -OH, and -F groups, indicating that terminations critically affect the polarization behavior of MXenes (Figure 7B) [78]. Consequently, the dipole moment can be precisely tailored by substituting MXene terminations with groups exhibiting different electronegativities and sizes. Furthermore, modulation of the Tx-site composition alters the work function and profoundly modifies carrier transport characteristics, as well as space charge region polarization within heterostructures (Figure 7C) [124]. Variations in the size of terminations during substitution simultaneously adjust the interlayer spacing (Figure 7D), thereby modifying interlayer hopping conductivity. This dual modulation of conductivity and polarization tailors the permittivity of MXenes, enabling precise control over their EM attenuation properties (Figure 7E).

A significant breakthrough involves the synthesis of halide-terminated MXenes (e.g., $Ti_3C_2Br_2$ and $Ti_3C_2Cl_2$) via molten salt etching [126], which enables controlled substitution [127]. The relatively weak Ti-Br and Ti-Cl bonds exhibit high substitution potential, permitting the grafting of diverse groups—including S, Se, Te, and amines (Figure 7F) [128]. Grafting polar organic groups offers a promising route to engineer abundant polarization sites directly on MXene surfaces, potentially enhancing polarization loss significantly. T_x-site replacement also critically

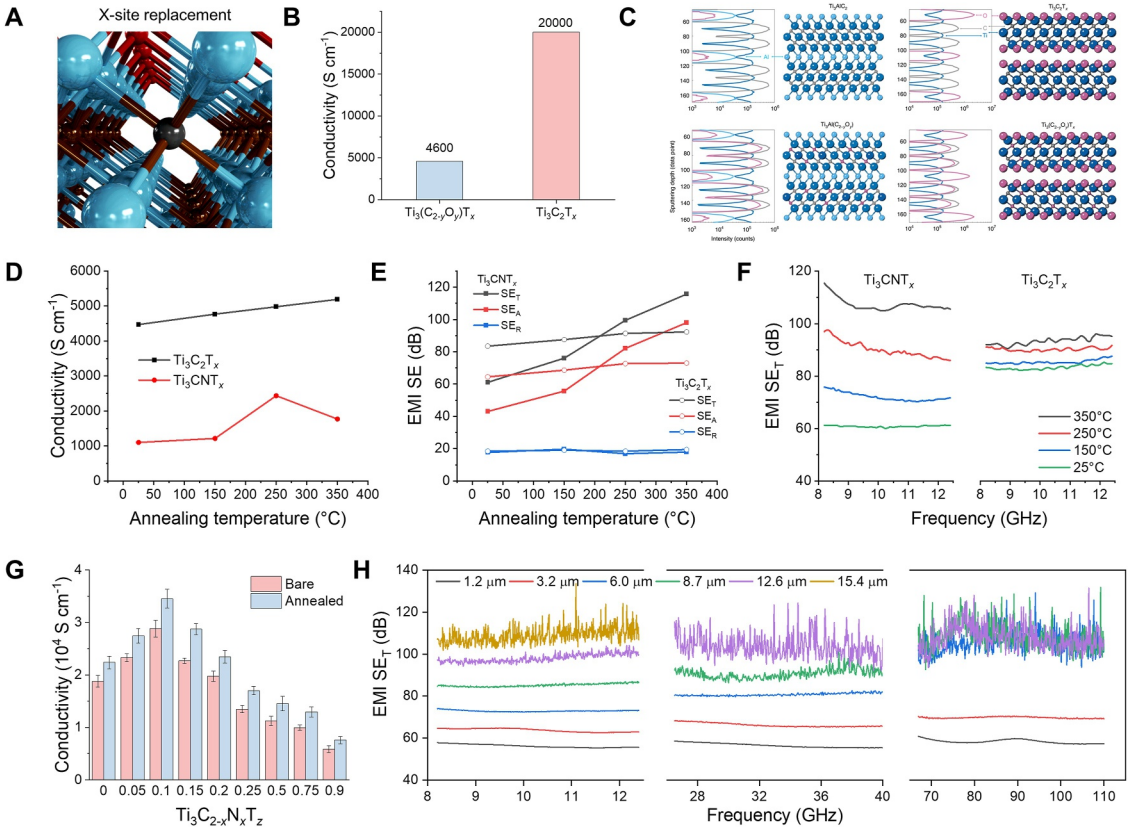

FIGURE 6 | Tuning the EM attenuation properties of MXenes via X-site substitution. (A) Schematic illustration of EM attenuation regulation through X-site replacement. (B) Electrical conductivity comparison of $Ti_3C_{2-y}O_yT_x$ [118] and $Ti_3C_2T_x$ [19]. (C) Depth profiles of Ti_3AlC_2 MAX and multilayer $Ti_3C_2T_x$ MXene via SIMS. Reproduced with permission from Ref. [119]. Copyright 2022, Springer Nature. (D) Conductivity and (E) EMI SE versus temperature of 40-μm Ti_3CNT_x and $Ti_3C_2T_x$ films. (F) EMI SE_T versus frequency of 40-μm Ti_3CNT_x and $Ti_3C_2T_x$ films. Reproduced with permission from Ref. [120]. Copyright 2020, American Association for the Advancement of Science. (G) Electrical conductivities of $Ti_3C_{2-x}N_xT_z$ before and after annealing. (H) EMI SE_T values of $Ti_3C_{1.9}N_{0.1}T_z$ films with varying thicknesses in the X-, Ka-, and W-bands. Reproduced with permission from Ref. [85]. Copyright 2025, Wiley-VCH.

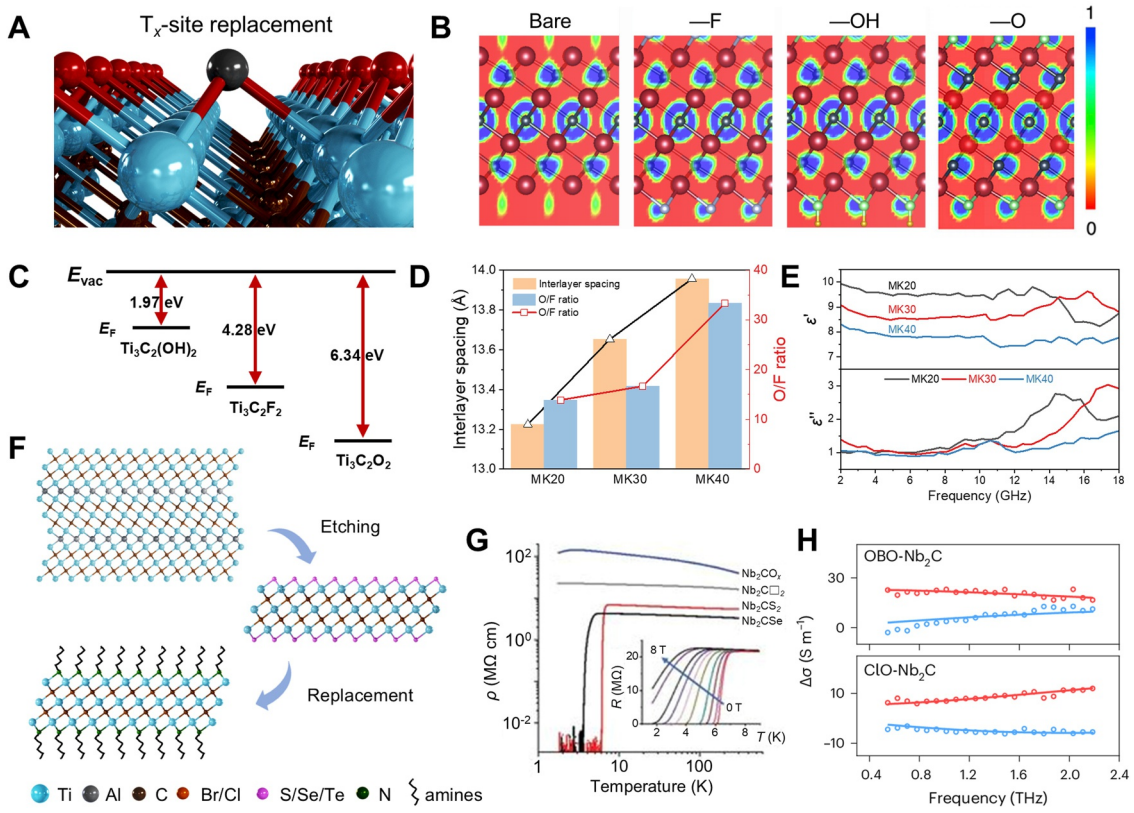

FIGURE 7 | Tuning the EM attenuation properties of MXenes via T_x-site substitution. (A) Schematic illustration of EM attenuation regulation through T_x-site replacement. (B) ELF of $V_4C_3T_x$ MXene with different terminations. Reproduced with permission from Ref. [78]. Copyright 2022, Elsevier. (C) Schematic diagram of the variation of the Fermi energy level and work function of $Ti_3C_2T_x$ with different terminations. (D) Comparison of the effects of different KOH concentration treatments on the layer spacing and O/F ratio. (E) KOH treatment of the EM parameters of $Ti_3C_2T_x$. Reproduced with permission from Ref. [124]. Copyright 2023, Wiley-VCH. (F) Schematic illustration of organic–inorganic hybrid MXene synthesis. (G) Temperature-dependent resistivity for the of Nb_2CT_x. Reproduced with permission from Ref. [24]. Copyright 2020, American Association for the Advancement of Science. (H) Terahertz photoconductivity of OBO-Nb_2C and ClO-Nb_2C. Reproduced with permission from Ref. [125]. Copyright 2024, Springer Nature.

influences electronic transport. For example, Nb_2CSe exhibits superconductivity at low temperatures (Figure 7G) [24]. In addition, for Nb_2C MXene with triatomic-layer borate polyanion terminations (OBO-Nb_2C), photoinduced terahertz conductivity follows the Drude model [125]. In contrast, chlorine/oxygen-terminated Nb_2C MXene (ClO-Nb_2C) exhibits behavior consistent with the Drude–Smith model (Figure 7H). The backscattering inherent in the Drude–Smith model impedes carrier transport, resulting in an order of magnitude higher terahertz mobility in OBO-Nb_2C compared to ClO-Nb_2C.

3.1.4 | Intralayer Regulation

Beyond intralayer modulation, interlayer interactions play a pivotal role in governing EM attenuation. This phenomenon is exemplified by low-temperature annealing, which enhances the electrical conductivity and EMI SE of MXene films through the removal of intercalants, thereby optimizing interlayer charge transport pathways [129].

Rakhmanov et al. [130] further investigated the influence of interlayer spacing and intercalants on EM attenuation mechanisms. Through spray-coating solutions containing distinct intercalants (e.g., TMAOH, TBAOH), they fabricated $Ti_3C_2T_x$ films with precisely controlled layer spacing, which is negatively correlated with the conductivity (Figure 8B). Notably, the measured sheet resistance exhibited significant deviation from theoretical predictions (Figure 8C), indicating that specific intercalant species may induce additional polarization mechanisms that further alter EM attenuation mechanisms.

By optimizing interlayer conductivity through conductive polymers, further enhancement of MXenes' EM shielding performance can be achieved (Figure 8D). MXenes' excellent intralayer conductivity is dominated by band-like transport, and the interlayer conductivity is primarily governed by hopping transport, limiting further performance improvement [133]. Shi et al. demonstrated that polymer anchoring (e.g., $PEDOT^{2+}$) on $Ti_3C_2T_x$ surfaces enables precise EM response modulation [61]. This approach achieves two counteractive effects: (1) reverse dipole alignment enhances interlayer conductivity and shielding efficiency, whereas (2) forward dipole orientation diminishes shielding performance. Remarkably, $PEDOT^{2+}$-modified films achieved an exceptional EMI SE_T of ~100 dB at 20 μm-thickness due to enhanced interlayer conductivity (Figure 8E,F). In addition, intercalant engineering permits controllable dipole

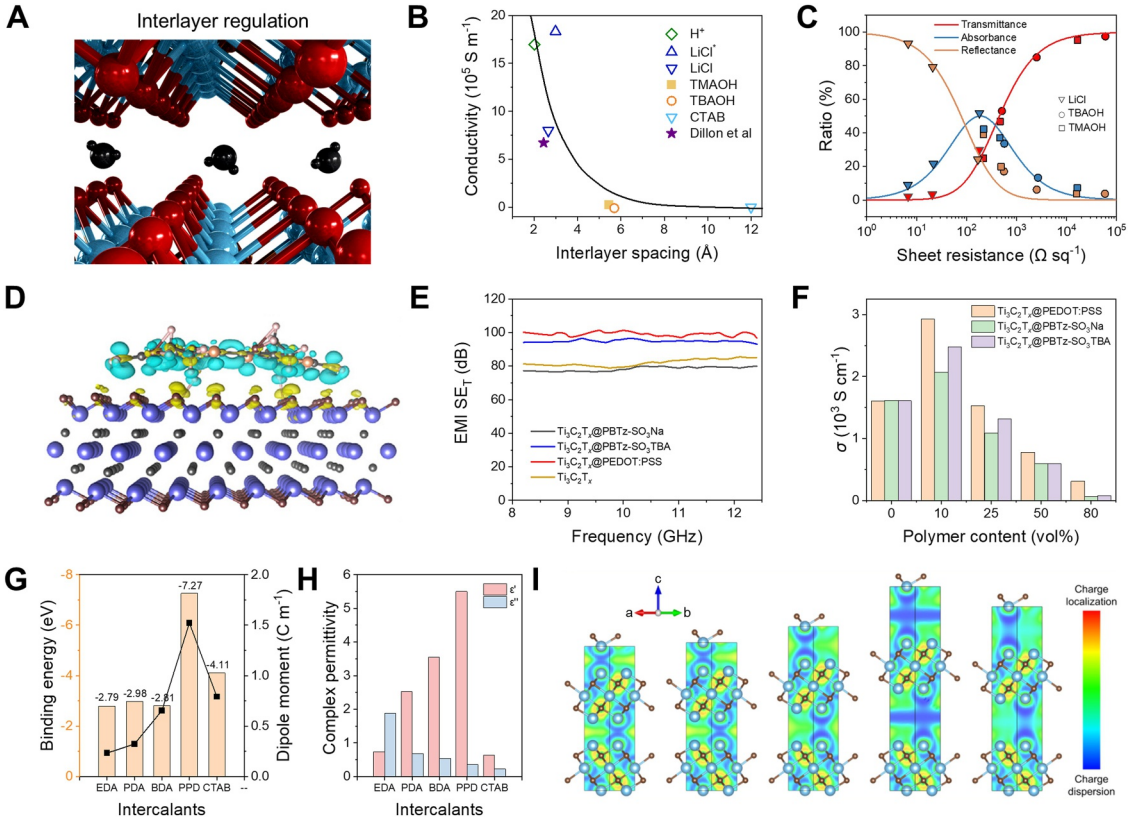

FIGURE 8 | Tuning the EM attenuation properties of MXenes via interlayer species substitution. (A) Schematic illustration of EM attenuation regulation through interlayer species replacement. (B) Electrical conductivity verse interlayer spacing of $Ti_3C_2T_x$ films delaminated with varying intercalants. (C) Reflectance (yellow line), absorptance (blue line), and transmittance (red line) of $Ti_3C_2T_x$ films delaminated with LiCl, TMAOH, and TBAOH. Reproduced with permission from Ref. [130]. Copyright 2025, Wiley-VCH. (D) Surface differential charge density of $Ti_3C_2T_x$@PEDOT: PSS. (E) EMI SE_T verse frequency for $Ti_3C_2T_x$@polymer (10:1). (F) Conductivity verse polymer content for $Ti_3C_2T_x$@polymer. Reproduced with permission from Ref. [131]. Copyright 2024, Elsevier. (G) Binding energy and dipole moment. (H) EM parameters of MXene aerogels with different intercalants. (I) ELF of the MXene aerogels with varying interlayer spacing. Reproduced with permission from Ref. [132]. Copyright 2025, American Chemical Society.

moment design to tune polarization loss (Figure 8G) [131]. Simultaneously, expanded interlayer spacing promotes oxidation of M-atoms, potentially inducing in-plane defects. These defects further generate dipoles and synergistically tune the dielectric constant (Figure 8H) [132]. When disregarding the direct contribution of intercalant species to charge transport, the influence of interlayer spacing variation on MXenes' intrinsic transport properties is revealed by the ELF. ELF analysis indicates reduced charge localization between M-atoms within M-M layers. This facilitates electron cloud migration from surface Ti atoms to subsurface C atoms, consequently modulating interlayer M-M resistance (Figure 8I).

3.1.5 | Film Fabrication

The structural characteristics of MXene films significantly influence EM attenuation, with these effects contingent upon various fabrication processes. The fabrication of sub-10-nm-thick MXene films has proven essential for effective EM attenuation application. In particular, neat (dense and without overlap) monolayer films that can be stacked layer by layer with controllable and uniform impedance characteristics have attracted increasing interest. This section summarizes the commonly used preparation techniques and attempts to analyze their potential effects on EM attenuation, although underlying mechanisms have not yet been fully revealed.

Vacuum filtration is the predominant method employed for the fabrication of micrometer-thick MXene films for EMI shielding. However, the fabrication of nanoscale films is feasible through the modulation of MXene concentration and can be transferred to rigid substrates [134]. Nonetheless, the inherent roughness of filter membranes and uncontrolled solvent evaporation often introduce wrinkles, cracks, and disordered stacking. These defects elevate surface roughness and are anticipated to intensify carrier scattering at boundaries, thereby diminishing electrical conductivity and conductive loss.

Dip coating facilitates the self-assembly of MXene nanosheets into continuous nanometer-thick films via intermolecular forces enabling layer-by-layer deposition [135, 136]. However, uncontrolled stacking of layers occurs during this process (Figure 9A). Moreover, repeated chemical modification introduces significant residual impurities, which promote scattering and reduce charge carrier mobility. The electronic structure can be also affected by the guest species, diminishing carrier concentration and thereby

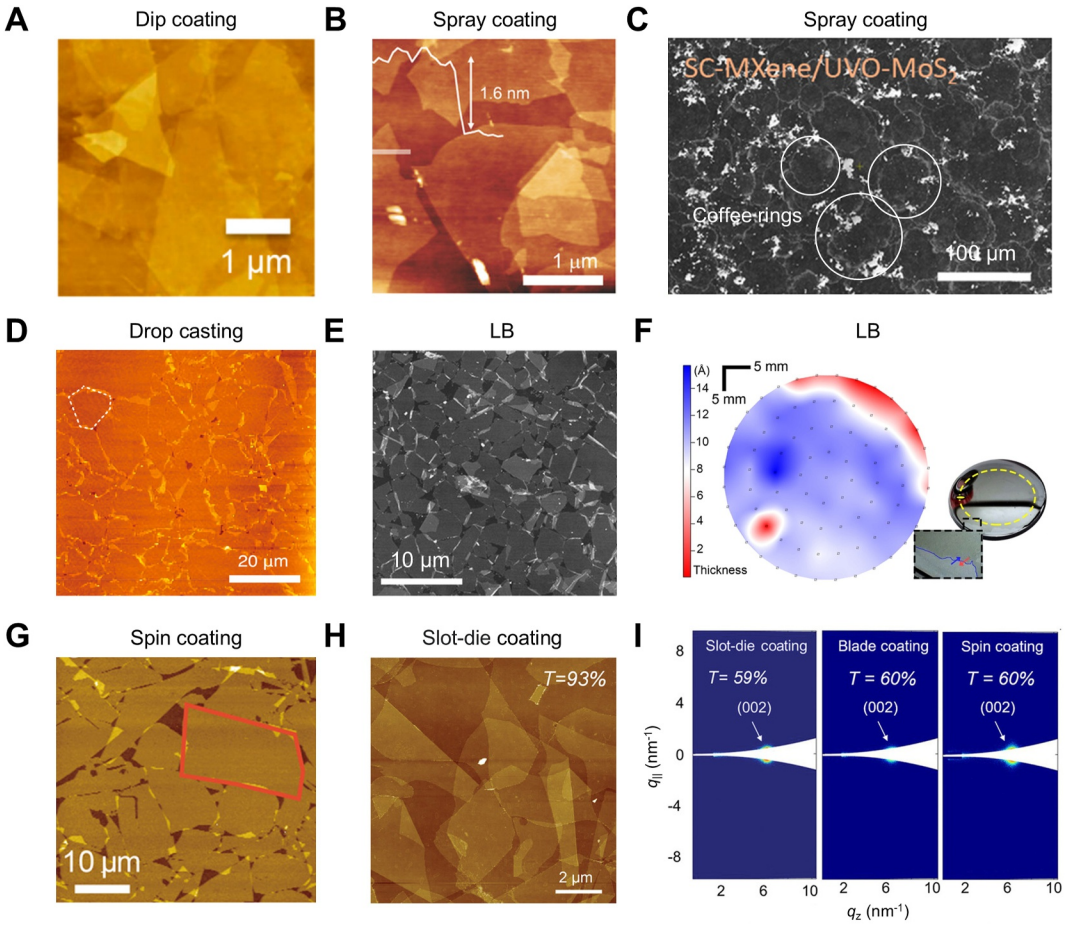

FIGURE 9 | The morphological characteristics of thin 2D films determined by the specific processing techniques by various approaches. (A) Atomic force microscopy (AFM) image of a $Ti_3C_2T_x$ film fabricated by dip coating. Reproduced with permission from Ref. [135]. Copyright 2019, American Chemical Society. (B) AFM image of a $Ti_3C_2T_x$ film prepared via spray coating. Reproduced with permission from Ref. [137]. Copyright 2018, Wiley-VCH. (C) Scanning electron microscope (SEM) image of a $Ti_3C_2T_x/MoS_2$ film produced by spray coating. Reproduced with permission from Ref. [138]. Copyright 2023, American Chemical Society. (D) AFM image of a $Ti_{0.87}O_2$ film processed by drop casting. Reproduced with permission from Ref. [139]. Copyright 2020, American Chemical Society. (E) AFM image of a $Ti_3C_2T_x$ film fabricated using the Langmuir–Blodgett (LB) technique. Reproduced with permission from Ref. [140]. Copyright 2021, American Chemical Society. (F) Ellipsometric mapping of a monolayer $Ti_3C_2T_x$ film prepared by the LB technique. (G) AFM image of $Ti_{0.87}O_2$ films processed by spin coating. Reproduced with permission from Ref. [141]. Copyright 2017, American Association for the Advancement of Science. (H) AFM image of $Ti_3C_2T_x$ films prepared via slot-die coating. Reproduced with permission from Ref. [142]. Copyright 2023, Wiley-VCH. (I) Grazing-incidence small-angle X-ray scattering (GISAXS) wedge plot showing the (002) peak over q_z. Reproduced with permission from Ref. [142]. Copyright 2023, Wiley-VCH. Reproduced with permission from Ref. [143]. Copyright 2023, American Chemical Society.

lowering conductive loss. Additional polar molecules may also introduce polarization sites, potentially enhancing polarization loss. Spray coating is a widely used technique for fabricating nanometric films (Figure 9B), leveraging the solution processability of MXene dispersions. Impedance can be tuned by adjusting the solution concentration or the number of coating passes [69]. However, this method requires an in situ evaporation and drying step—a complex and often unpredictable nonequilibrium process that leads to difficult-to-control film structures. According to the profile evolution theories, drying can occur via constant radius regime (CRR), constant contact angle regime (CCAR), or mixed modes [144], accompanied by Marangoni [145] and capillary flows [146]. These flows drive internal mass transfer, leading to nonuniform deposition and poor nanosheet orientation [138]. Secondary-electron SEM images clearly show coffee-stain patterns, indicative of impurity accumulation (Figure 9C). Furthermore, the in situ heating involved accelerates oxidation, hindering the conductivity of MXenes. Drop-casting, akin to spraying with larger droplets, often suffers from uncontrolled mass transfer effects, making it challenging to produce neat films. However, these forces can be actively modulated through chemical assistance, enabling the fabrication of uniform films with tunable layer (Figure 9D) [139, 147].

Enhancing interflake interactions presents an alternative strategy to counteract forces during evaporation, which can be achieved through LB assembly [148]. The LB technique is a method for assembling molecularly ordered thin films at the air–liquid interface, utilizing amphiphilic molecules to achieve precise monolayer formation. By applying mechanical compression to modulate surface pressure, the LB technique enables the formation of neat MXene films (Figure 9E,F). The

resulting enhanced interflake cohesion partially mitigates structural damage induced by evaporation. Furthermore, external mechanical compression can be substituted by Marangoni forces driven by low-surface-tension liquids, thereby simplifying the fabrication process. However, interflake interactions remain limited, often complicating uniform deposition on high-surface-energy substrates. This limitation may be overcome using advanced Langmuir–Schaefer (LS) deposition, which bypasses evaporation through direct substrate adhesion, thereby preserving structural integrity [149]. Additionally, the requirement for amphiphilicity often necessitates chemical modifiers, such as ethyl acetate (EA) [150] or tetrabutylammonium hydroxide (TBAOH) [151], to tailor hydrophilicity and promote effective interfacial accumulation of MXene nanosheets. Although beneficial for assembly, these additives can compromise interflake electrical conductivity and enhance polarizability, leading to increased dielectric loss.

Shear-assisted coating enables rapid fabrication of films with enhanced alignment, which facilitates the formation of well-organized conductive pathways. As an example, spin coating can rapidly yield MXene films of tunable thickness on flat substrates by controlling the solution concentration, despite significant material loss [152, 153]. Moreover, the fabrication of monolayer neat films through spin coating (Figure 9G) depends on external chemical agents that influence EM loss characteristics, as previously mentioned [141, 154]. In contrast, slot-die coating (Figure 9H) [142] and blade coating [80] also enable the deposition of highly oriented films. These techniques have demonstrated notable advantages for transparent conductive films, offering improved alignment (Figure 9I), absence of chemical contamination, and minimal material waste. Nevertheless, uncontrolled layer stacking remains a challenge, hindering the reproducible fabrication of monolayer neat films [143]. A comprehensive comparison of different preparation processes for nano-thick films is summarized in Table 3.

3.2 | Dynamic Modulation

Compared to statical adjusting, dynamic modulation strategies can adjust EM parameters in real time to regulate the EM attenuation characteristics, facilitating advanced and intelligent applications [157–159], such as active stealth [160], reconfigurable intelligent surface (RIS) [161], and wireless communications [162]. Thermal, electrical, and optical excitation are typical physical approaches to modulate EM attenuation [163]. These techniques have attracted significant interest for their capacity to modify carrier concentration and transport dynamics, thereby tailoring EM responses toward enhanced performance [164].

Thermal heating typically exhibits millisecond-scale response times [165, 166]. The electrical conductivity of metallic MXenes generally decreases with rising temperature, whereas that of semiconducting MXenes increases [133, 167]. However, for EM absorbers, the appropriate impedance makes hopping conduction typically governs charge transport. Consequently, conductive loss increases with temperature (Figure 10A) [168]. Simultaneously, elevated temperatures enhance molecular thermal agitation, facilitating dipole reorientation and lowering the energy barrier for dipole rotation. These factors accelerate Debye relaxation, profoundly altering microwave dielectric loss behavior (Figure 10B,C). The shortened polarization relaxation time shifts the relaxation frequency toward lower frequencies, inducing stronger dielectric losses within the target frequency, facilitating broadband effective absorption across the desired frequency range.

Electrical gating demonstrates nanosecond-scale response times [174, 175], enabling precise EM response manipulation through dielectric-induced carrier generation (10^{13}–10^{14} cm^{-2}) and Fermi level manipulation. This process fundamentally changes the charge transport behavior through inter-band or intra-band

TABLE 3 | Summary of the characteristics of different deposition methods.

			Spin coating				Drop casting		
	Vacuum filtration and transfer	Spray coating	Direct	Chemical assistance	Blade/Slot-die coating	Dip coating	Direct	Chemical assistance	LB/LS
Neat monolayer tiling	×	×	×	○	×	×	×	○	○
Alignment	△	×	○	○	○	×	×	○	○
Clean	○	○	○	×	○	×	○	×	×
Low waste	○	○	×	×	○	×	○	○	△
Conductive loss	↓	↓	—	↓↓	—	↓↓	↓	↓↓	↓↓
Polarization loss	—	—	—	↑	—	↑	—	↑	↑
References	[134, 155]	[69, 130, 137]	[153, 156]	[141, 154]	[113, 142, 143]	[135, 136]	[92, 138]	[139, 147]	[93, 107, 140, 149]

Note: ○ represents good, △ represents medium, and × represents bad. ↓represents decrease, ↓↓represents significant decrease, - represents no significant change, and ↑ represents improvement.

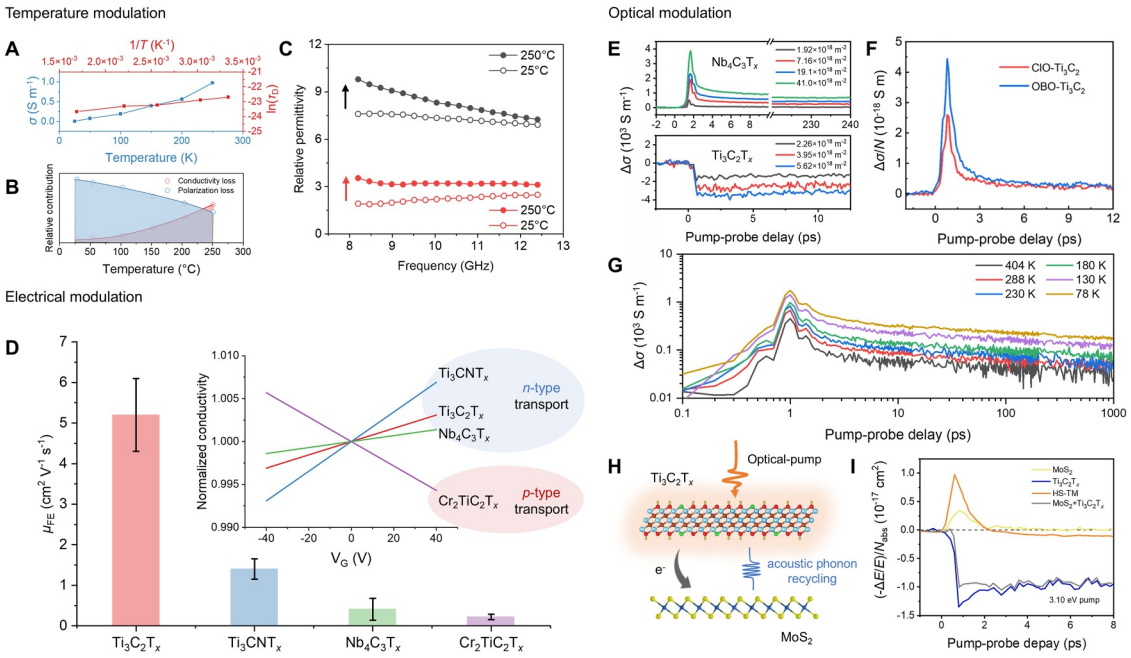

FIGURE 10 | Dynamic modulation of MXene–EM wave interactions via thermal, electrical, and optical excitation. (A) Temperature-dependent ln (τ_D) and σ fitted by Debye theory, (B) relative contribution of polarization loss and conductivity loss, and (C) temperature-dependence complex relative permittivity of $Ti_3C_2T_x$ MXene/aramid nanofiber (ANF)/polyimide (PI) aerogels. Reproduced with permission from Ref. [168]. Copyright 2022, Elsevier. (D) Field-effect mobility of single-flake $Ti_3C_2T_x$ [169], Ti_3CNT_x [170], $Nb_4C_3T_x$ [171], and $Cr_2TiC_2T_x$ [172], and the (inset) normalized conductivity verse gate voltage. (E) Time-resolved $\Delta\sigma$ of $Nb_4C_3T_x$ and $Ti_3C_2T_x$, and (G) temperature-dependent terahertz $\Delta\sigma$ of $Nb_4C_3T_x$. Reproduced with permission from Ref. [133]. Copyright 2022, Springer Nature. (F) Time-resolved $\Delta\sigma$ of ClO-$Ti_3C_2T_x$ and OBO-$Ti_3C_2T_x$. Reproduced with permission from Ref. [125]. Copyright 2024, Springer Nature. (H) Schematic illustration of MXene interact with MoS_2 under optical pump. (I) Terahertz photoconductivity dynamics normalized by absorbed photon density of $Ti_3C_2T_x$, MoS_2, and the heterostructure under 3.10 eV excitations. Reproduced with permission from Ref. [173]. Copyright 2025, American Chemical Society.

transitions, thereby modifying EM interaction characteristics [176]. Graphene has emerged as a benchmark material in this domain, where efficient modulation has been achieved owing to its high mobility resulting from the unique band structure [160, 177]. However, long electron relaxation times induce a frequency-dependent dispersion of the conductivity [15], imposing significant limitations in the high-frequency terahertz region. In contrast, MXenes show potential for broadband EM modulation, yet their efficacy in gate-controlled EM tuning is currently limited by their low field-effect mobility (Figure 10D). Although developing high-mobility MXenes appears promising to solve the problem [178–182], precise synthesis remains challenging.

All-optical modulation exhibits the fastest intrinsic response speeds among the three ways, reaching femtosecond timescales [183]. Optical pump–terahertz probe (OPTP) spectroscopy enables rapid capture of terahertz responses in photoexcited materials. Under optical pumping, high-energy carriers evolve into hot carriers through the carrier–carrier scattering within hundreds of femtoseconds [184]. These hot carriers subsequently relax through carrier-phonon coupling interactions with optical and acoustic phonons. Throughout this process, the material's interaction with terahertz radiation dynamically evolves. MXenes display composition-dependent carrier–phonon coupling due to various electron density of states near the Fermi surface and the matching between electron and phonon energy levels [185, 186], enabling diverse photoresponses. $Ti_3C_2T_x$ and $Nb_4C_3T_x$ exhibit positive and negative photoconductivity ($\Delta\sigma$; Figure 10E), respectively, attributable to hot-carrier thermalization and interband transitions [133]. Crucially, despite sharing similarly ultrafast (fs-scale) carrier-carrier scattering, their carrier relaxation times differ markedly: $Nb_4C_3T_x$ relaxes within picoseconds, whereas $Ti_3C_2T_x$ requires nanoseconds. Consequently, ClO- and OBO- terminated Ti_3C_2 enable accelerated relaxation (Figure 10F) [125], confirming that composition tailoring and dynamic modulation synergistically regulating EM attenuation behavior. Optical stimulation can work synergistically with temperature. At low temperatures, phonon scattering is reduced and the thermalized carriers induces a higher $\Delta\sigma$ (Figure 10G). In addition, the relaxation process is expected to be accelerated through MXene/semiconductor interface interactions, including high-energy carriers transfer and acoustic phonon recycling (Figure 10H,I) [173].

Beyond conventional physical modulation strategies, integrating interlayer and surface chemistry enable 2D materials better modulation depth and fancy properties. Tang et al. [187] studied the dynamic influence of intercalants on the resistivity of MXenes. The resistance of $Ti_3C_2T_x$ continued to decrease in the dry argon flow and finally stabilized at 72% of the initial resistance value. Passing a wet argon flow can restore this resistance value, indicating that the H_2O intercalation/deintercalation process is reversible. For MXene films whose resistance is dominated by interlayer resistance, near-infrared laser irradiation can further remove water or organic intercalants and

further reduce the resistance (Figure 11A,B). These findings establish the critical role of interlayer and surface guest species in governing electronic transmission properties, yet precise control pathways remain necessary. Ionic gating offers a highly controllable approach for this regulation mechanism, enabling voltage-driven manipulation of guest species interactions with the material, and thus achieving tunable EM attenuation [190]. The large electric double layer (EDL) capacitance and pseudocapacitance enable ionic gating to induce sheet carrier densities exceeding ~10^{14} cm^{-2}, surpassing conventional dielectric gating by 1–3 orders of magnitude [191].This phenomenon enables materials to undergo fundamental phase transitions from insulating to metallic states, and even to superconducting phases [192], and significantly modulates plasmonic responses in gold [193].Guest species intercalation further alters coordination numbers and crystal field environments [194, 195], with consequent modifications to electronic structure profoundly reshaping EM attenuation characteristics of 2D layered materials.

The combination of metal conductivity and redox charge storage endows MXenes unique characteristics in response to incident EM waves and allows EM response to be regulated. Han et al. [188] actively modulated MXenes' response to EM waves via electrochemically driven ion intercalation and deintercalation (Figure 11C,D), which leads to changes in charge transfer, the oxidation state of the transition metal, and interlayer spacing (Figure 11E). The interaction of MXenes with microwaves changes with the applied potentials. The redox peak indicates that the oxidation state of the M-site element changes during the intercalation and deintercalation process, and affect the conductivity and the EMI shielding characteristics of the MXene film (Figure 11F) [196–198]. Dynamic modulation of materials through intercalation/deintercalation of intercalants changes the electronic structure, which will have a major impact on the conductive loss, thus allowing it to work in the microwave to terahertz bands. Fei et al. [189] further optimized device performance by integrating parallel metal electrodes to improve compactness and refining electrolyte/film impedance for superior modulation (Figure 11G,H). Coupling this device with a Salisbury screen achieved a substantial reflection modulation depth of ~20 dB (Figure 11I,J).

Finally, we summarize the differences in modulation mechanisms and materials. Figure 12A compares the typical response times of various modulation approaches [160, 165, 166, 174, 175, 183, 199–204]. Among these, electric-field-based modulation has attracted considerable interest owing to its precision and ease of operation. The relationship between induced carrier concentration and time is estimated and summarized in Figure 12B. Although ionic gating exhibits distinct advantages under extended response-time conditions, dielectric gating remains more commonly employed in high-speed applications due to its faster switching performance. Figure 12C compares the EM

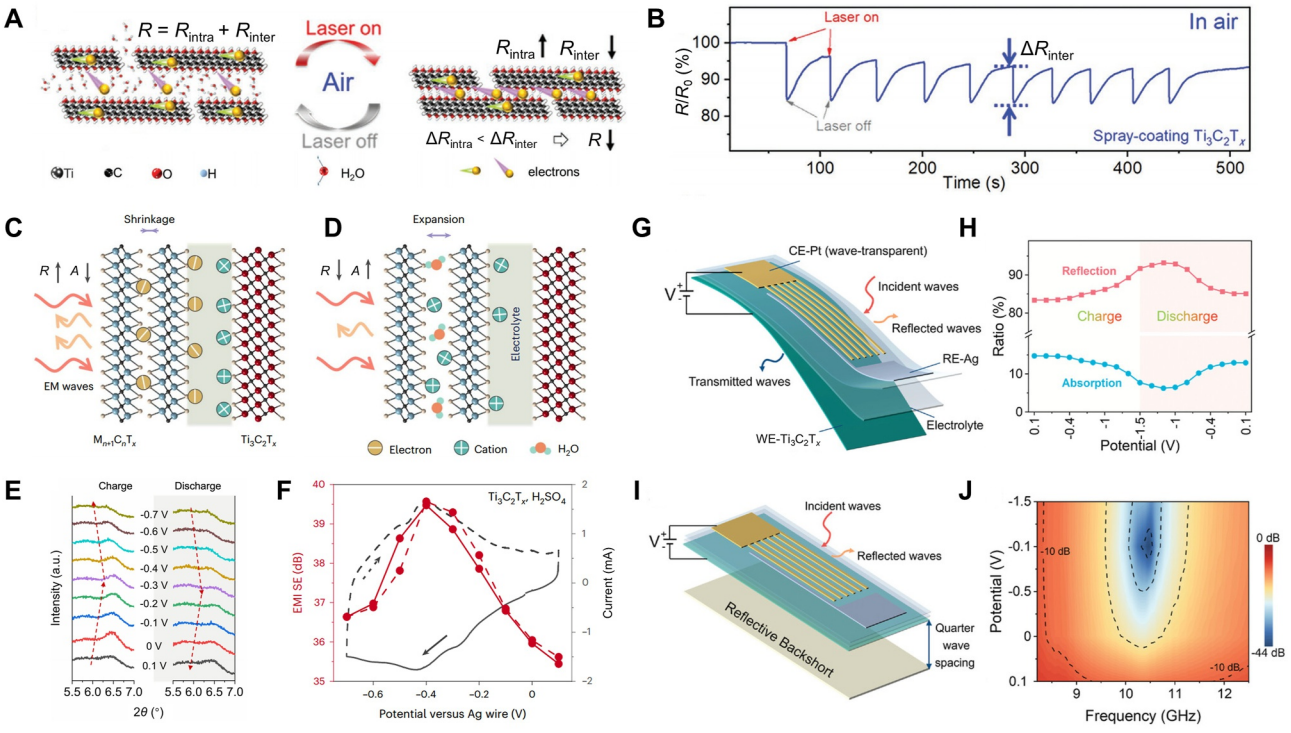

FIGURE 11 | Dynamic modulation of MXene–EM wave interactions via guest species. (A) Schematic illustration of the resistance changes of $Ti_3C_2T_x$ induced by laser. (B) Time-resolved resistance changes of $Ti_3C_2T_x$ induced by laser. Reproduced with permission from Ref. [187]. Copyright 2022, Wiley-VCH. (C,D) Schematic illustration of electrochemically modulated interaction of MXenes with EM waves during (C) deintercalation and (D) intercalation. (E) In situ XRD patterns of the film with $Ti_3C_2T_x$ electrode in 1 M H_2SO_4. (F) Dynamic EMI SE_T and the CVs of the device using a $Ti_3C_2T_x$ electrode in 1 M H_2SO_4. Reproduced with permission from Ref. [188]. Copyright 2023, Springer Nature. (G) Schematic diagram of a tunable EM attenuator based on parallel metals and $Ti_3C_2T_x$ electrode and (H) the corresponding extracted variation in reflection and absorption. (I) Schematic diagram of a $Ti_3C_2T_x$-based EM attenuator in combination with Salisbury screen and (J) the corresponding RL map. Reproduced with permission from Ref. [189]. Copyright 2024, Wiley-WCH.

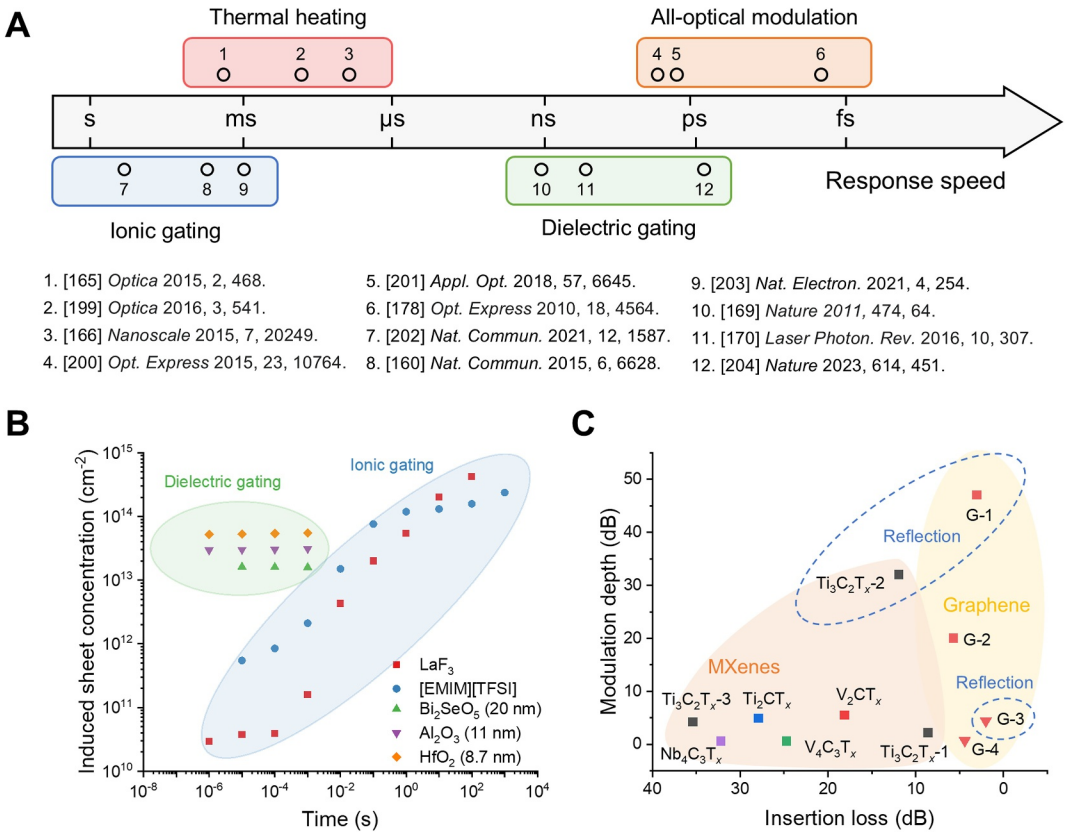

FIGURE 12 | Comparison of various dynamic modulation strategies. (A) Schematic illustration of response speed and modulation methods. The data are adapted from refs. [160, 165, 166, 174, 175, 183, 199–204]. (B) Estimated induced sheet concentration verse time for dielectric gating and ionic gating. The data sources are as follows: LaF_3 [205], [EMIM][TFSI] [206], Bi_2SeO_5 [207], Al_2O_3, and HfO_2 [208]. (C) Modulation depth verse insertion loss of MXenes and graphene. The data sources are as follows: G-1 [160], G-2 [209], G-3 [210], G-4 [176], $Ti_3C_2T_x$-1 and $Ti_3C_2T_x$-2 [189], $Ti_3C_2T_x$-3 and other MXenes [188].

modulation performance between MXenes and graphene (typical EM modulation materials). Currently, in the regulation of transmission signals, ionic-gated (square points) MXene offers a higher modulation depth than dielectric-gated graphene (inverted triangle), yet remains lower than that of ionic-gated graphene. Although a reflection-mode configuration based on the Salisbury screen mitigates this gap, higher insertion loss of MXenes implying a reduced upper limit for the strength of controllably modulated signals. In summary, although MXene shows application potential for intelligent regulation, there is still a gap in performance, which is expected to be solved through the development of new MXene materials.

4 | Conclusions and Perspectives

In summary, MXenes exhibits tunable EM attenuation performance in the microwave and terahertz bands, demonstrating great potential as ultra-lightweight high-efficiency EM shielding and absorption materials. $Ti_3C_2T_x$ surpasses gold in specific shielding effectiveness (SSE/t), whereas $Ti_3C_{1.9}N_{0.1}T_x$ exceeds copper's EMI SE_T at equivalent thicknesses. Enabled by ultrashort carrier scattering times and high carrier densities, $Ti_3C_2T_x$ achieves broadband film impedance matching at nanoscale thicknesses.

When used as absorbers, the large specific surface area of MXenes promotes the formation of conductive networks, the highly oriented random functional groups provide high polarization intensity, and outstanding tunability helps adjust conductive loss and polarization loss, potentially enabling thin and lightweight planar EM absorbers. The unique intercalation-mediated EM attenuation mechanism further suggests potential for intelligent EM modulators. Although critical for next-generation 6G technologies, realizing this potential demands advances in MXene synthesis and fundamental understanding.

4.1 | Precise Etching Process for High-Performance MXenes

Defect-free high-quality MXenes are advantageous for enhancing electrical transport properties and are expected to significantly improve conductive loss, thereby promoting higher EMI SE and optimized intrinsic absorption in MXene nanofilms. Currently, $Ti_3C_{1.9}N_{0.1}T_x$ has achieved a notable electrical conductivity of approximately 35,000 S cm^{-1}. However, the introduction of defects during etching (particularly under high nitrogen content) limits further enhancement in conductivity. Addressing this issue requires advanced etching strategies that

enable precise control over etching thermodynamics and kinetics. Electrochemical etching, for instance, offers a promising approach by enabling accurate regulation of reaction activity through applied voltage, thereby facilitating the synthesis of high-quality MXenes with minimal defects.

4.2 | Synthesis of High-Mobility MXenes for Intelligent EM Applications

Owing to their relatively low carrier mobility, MXenes exhibit limited modulation capability under a given induced areal carrier density, primarily due to insufficient modulation in electrical conductivity. Although ionic gating offers an effective means of carrier-density tuning, it suffers from slow response characteristics and inevitably introduces substantial insertion losses caused by dipole polarization and ionic conduction within the electrolyte. Topological insulator MXenes, such as $Mo_2TiC_2O_2$, show considerable promise for enabling high-speed and highly sensitive dynamic EM modulation. Previously predicted topological insulator MXenes predominantly feature pure terminations [178–181], yet synthesizing specific pure terminated MXenes remains challenging.

4.3 | Uncovering Ultra-Broadband EM Attenuation Mechanisms in MXenes

The broad distribution of relaxation timescales comprehensive analysis of loss mechanisms through narrowband spectroscopy, limiting the rational design of ultra-broadband absorbers. Moreover, the millimeter-wave frequency range appears to encompass critical polarization relaxation processes within MXenes, which are essential for a deeper understanding of their EM attenuation behavior. Elucidating the interaction mechanisms between MXenes and EM waves across a wide spectrum will enable multi-frequency polarization engineering via tailored surface terminations, offering a strategy for achieving high-performance broadband absorption.

Author Contributions

Guozheng Zhang: visualization, writing – original draft, writing – review and editing. **Sitong Li:** visualization, writing – review and editing. **Libo Chang:** investigation, writing – review and editing. **Zelin Zhao:** writing – review and editing. **Tianze Zhang:** writing – review and editing. **Si Chen:** supervision, writing – review and editing. **Xuehang Wang:** writing – review and editing. **Zhe Wu:** writing – review and editing. **Tianpeng Ding:** supervision, writing – review and editing. **Xu Xiao:** supervision, writing – review and editing.

Acknowledgments

This work was financially supported by the National Key Research and Development Program of China (Grant No. 2023YFB3811300), the National Natural Science Foundation of China (Grant No. 52202084), the Outstanding Scholarship Foundation of UESTC (Grant No. A1098531023601345), Sichuan Science and Technology Support Program (Grant No. 2021JDTD0026), the Natural Science Foundation of Sichuan Province (Grant Nos. 2023NSFSC0437 and 2023NSFSC0959), the Natural Science Foundation of Sichuan Province (Grant No. 2024NSFSC0997), and the Postdoctoral Fellowship Program of CPSF (Grant No. GZC20230383).

Conflicts of Interest

The authors declare no conflicts of interest.

Data Availability Statement

The data that support the findings of this study are available from the corresponding author upon reasonable request.

References

1. M. Moussaoui, E. Bertin, and N. Crespi, "5G Shortcomings and Beyond-5G/6G Requirements," in *2022 1st International Conference on 6G Networking (6GNet)* (IEEE, 2022), 1–8, https://doi.org/10.1109/6GNet54646.2022.9830439.

2. H. H. H. Mahmoud, A. A. Amer, and T. Ismail, "6G: A Comprehensive Survey on Technologies, Applications, Challenges, and Research Problems," *Transactions on Emerging Telecommunications Technologies* 32, no. 4 (2021): e4233, https://doi.org/10.1002/ett.4233.

3. M. Chowdhury, M. Shahjalal, M. Hasan, and Y. Jang, "The Role of Optical Wireless Communication Technologies in 5G/6G and IoT Solutions: Prospects, Directions, and Challenges," *Applied Sciences* 9, no. 20 (2019): 4367, https://doi.org/10.3390/app9204367.

4. H. Tataria, M. Shafi, M. Dohler, and S. Sun, "Six Critical Challenges for 6G Wireless Systems: A Summary and Some Solutions," *IEEE Vehicular Technology Magazine* 17, no. 1 (2022): 16–26, https://doi.org/10.1109/MVT.2021.3136506.

5. H. Tataria, M. Shafi, A. Molisch, M. Dohler, H. Sjöland, and F. Tufvesson, "6G Wireless Systems: Vision, Requirements, Challenges, Insights, and Opportunities," *Proceedings of the IEEE* 109, no. 7 (2021): 1166–1199, https://doi.org/10.1109/JPROC.2021.3061701.

6. F. Shahzad, M. Alhabeb, C. Hatter, et al., "Electromagnetic Interference Shielding With 2D Transition Metal Carbides (MXenes)," *Science* 353, no. 6304 (2016): 1137–1140, https://doi.org/10.1126/science.aag2421.

7. X. Li, X. Yin, C. Song, et al., "Self-Assembly Core-Shell Graphene-Bridged Hollow MXenes Spheres 3D Foam With Ultrahigh Specific EM Absorption Performance," *Advanced Functional Materials* 28, no. 41 (2018): 1803938, https://doi.org/10.1002/adfm.201803938.

8. R. Che, J. Gu, J. Kong, et al., "Designing Future Nanomaterials for Electromagnetic Wave Absorption and Shielding," *Cell Reports Physical Science* 6, no. 3 (2025): 102502, https://doi.org/10.1016/j.xcrp.2025.102502.

9. L. Yao, J. Shu, J. Zhao, J. Zong, M. Cao, and W. Cao, "Heterodimensional Structure Integrating Electromagnetic Functions and Hybrid Energy Storage to Drive Multifunctional Devices," *Advanced Functional Materials* 35, no. 31 (2025): 2503307, https://doi.org/10.1002/adfm.202503307.

10. Y. Wu, S. Tan, Y. Zhao, L. Liang, M. Zhou, and G. Ji, "Broadband Multispectral Compatible Absorbers for Radar, Infrared and Visible Stealth Application," *Progress in Materials Science* 135 (2023): 101088, https://doi.org/10.1016/j.pmatsci.2023.101088.

11. T. Zhao, H. Wan, T. Zhang, and X. Xiao, "Mechanism of the Terahertz Wave–MXene Interaction and Surface/Interface Chemistry of MXene for Terahertz Absorption and Shielding," *Accounts of Chemical Research* 57, no. 15 (2024): 2184–2193, https://doi.org/10.1021/acs.accounts.4c00326.

12. Z. Gao, A. Iqbal, T. Hassan, S. Hui, H. Wu, and C. Koo, "Tailoring Built-In Electric Field in a Self-Assembled Zeolitic Imidazolate Framework/MXene Nanocomposites for Microwave Absorption," *Advanced*

Materials 36, no. 19 (2024): 2311411, https://doi.org/10.1002/adma.202311411.

13. Y. Fei, X. Y. Wang, F. Wang, W. K. Xie, Q. Y. Wen, and X. Xiao, "Covalent Coupling Induced-Polarization Relaxation in MXene-based Terahertz Absorber for Realizing Dual Band Absorption," *Chemical Engineering Journal* 461 (2023): 142049, https://doi.org/10.1016/j.cej.2023.142049.

14. W. Xie, Q. Tang, J. Xie, et al., "Organohydrogel-Based Transparent Terahertz Absorber via Ionic Conduction Loss," *Nature Communications* 15, no. 1 (2024): 38, https://doi.org/10.1038/s41467-023-44344-2.

15. P. Pham, W. Zhang, N. Quach, et al., "Broadband Impedance Match to two-dimensional Materials in the Terahertz Domain," *Nature Communications* 8, no. 1 (2017): 2233, https://doi.org/10.1038/s41467-017-02336-z.

16. M. Han, X. Yin, H. Wu, et al., "Ti_3C_2 MXenes With Modified Surface for High-Performance Electromagnetic Absorption and Shielding in the X-band," *ACS Applied Materials & Interfaces* 8, no. 32 (2016): 21011–21019, https://doi.org/10.1021/acsami.6b06455.

17. W. Shui, J. Li, H. Wang, et al., "$Ti_3C_2T_x$ MXene Sponge Composite as Broadband Terahertz Absorber," *Advanced Optical Materials* 8, no. 21 (2020): 2001120, https://doi.org/10.1002/adom.202001120.

18. M. Naguib, M. Kurtoglu, V. Presser, et al., "Two-Dimensional Nanocrystals Produced by Exfoliation of Ti_3AlC_2," *Advanced Materials* 23, no. 37 (2011): 4207–4207, https://doi.org/10.1002/adma.201190147.

19. T. Mathis, K. Maleski, A. Goad, et al., "Modified MAX Phase Synthesis for Environmentally Stable and Highly Conductive Ti_3C_2 MXene," *ACS Nano* 15, no. 4 (2021): 6420–6429, https://doi.org/10.1021/acsnano.0c08357.

20. N. Tzenov and M. Barsoum, "Synthesis and Characterization of Ti_3AlC_2," *Journal of the American Ceramic Society* 83, no. 4 (2000): 825–832, https://doi.org/10.1111/j.1151-2916.2000.tb01281.x.

21. M. Barsoum and T. El-Raghy, "Synthesis and Characterization of a Remarkable Ceramic: Ti_3SiC_2," *Journal of the American Ceramic Society* 79, no. 7 (1996): 1953–1956, https://doi.org/10.1111/j.1151-2916.1996.tb08018.x.

22. D. Cuskelly, E. Richards, E. Kisi, and V. Keast, "Ti_3GaC_2 and Ti_3InC_2: First Bulk Synthesis, DFT Stability Calculations and Structural Systematics," *Journal of Solid State Chemistry* 230 (2015): 418–425, https://doi.org/10.1016/j.jssc.2015.07.028.

23. Y. Li, H. Shao, Z. Lin, et al., "A General Lewis Acidic Etching Route for Preparing MXenes With Enhanced Electrochemical Performance in Non-Aqueous Electrolyte," *Nature Materials* 19, no. 8 (2020): 894–899, https://doi.org/10.1038/s41563-020-0657-0.

24. V. Kamysbayev, A. Filatov, H. Hu, et al., "Covalent Surface Modifications and Superconductivity of Two-Dimensional Metal Carbide MXenes," *Science* 369, no. 6506 (2020): 979–983, https://doi.org/10.1126/science.aba8311.

25. M. Downes, C. Shuck, R. Lord, et al., "M_5X_4: A Family of MXenes," *ACS Nano* 17, no. 17 (2023): 17158–17168, https://doi.org/10.1021/acsnano.3c04967.

26. H. Ding, Y. Li, M. Li, et al., "Chemical Scissor-Mediated Structural Editing of Layered Transition Metal Carbides," *Science* 379, no. 6637 (2023): 1130–1135, https://doi.org/10.1126/science.add5901.

27. K. Kazemi, E. Hosseini, S. Hu, et al., "MXene Membrane in Planar Microwave Resonant Structures for 5G Applications," *Applied Materials Today* 26 (2022): 101294, https://doi.org/10.1016/j.apmt.2021.101294.

28. Q. Liu, Q. Cao, L. C. Bi, et al., "CoNi@SiO_2@TiO_2 and CoNi@Air@TiO_2 Microspheres With Strong Wideband Microwave Absorption," *Advanced Materials* 28, no. 3 (2015): 486–490, https://doi.org/10.1002/adma.201503149.

29. G. Wu, Y. Cheng, Z. Yang, et al., "Design of Carbon Sphere/Magnetic Quantum Dots With Tunable Phase Compositions and Boost Dielectric Loss Behavior," *Chemical Engineering Journal* 333 (2018): 519–528, https://doi.org/10.1016/j.cej.2017.09.174.

30. J. Wang, M. Xia, J. Sun, et al., "Hybrid Bilayers of Carbon/$NiBr_2$ Anchoring on FeSiB Surface for Enhanced Microwave Absorption Coupling With Smart Discoloration," *Rare Metals* 44, no. 1 (2025): 489–502, https://doi.org/10.1007/s12598-024-02913-4.

31. A. Pawar, D. Sonawane, K. Erande, and D. Derle, "Terahertz Technology and Its Applications," *Drug Invention Today* 5, no. 2 (2013): 157–163, https://doi.org/10.1016/j.dit.2013.03.009.

32. J. Zong and M. Cao, "Graphene-Like MXene-Based Microwave Absorbers and Shields: Latest Progress and Perspectives," *Materials Today Physics* 43 (2024): 101400, https://doi.org/10.1016/j.mtphys.2024.101400.

33. J. Zong, H. Zhai, H. Guan, Z. Wang, M. Cao, and W. Cao, "Host-Guest Engineered Electromagnetic Fabrics With Controllable Polarization-Conduction Network for Multispectral Stealth and Wireless Actuation," *Advanced Functional Materials* (2025): e07277, https://doi.org/10.1002/adfm.202507277.

34. C. Wang, Y. Feng, J. Zhou, G. Wen, and L. Xia, "Numerical Analysis, Experimental Verification and Criterion Establishment of Non-Magnetic Microwave Absorbing Material," *Journal of Colloid and Interface Science* 613 (2022): 256–264, https://doi.org/10.1016/j.jcis.2022.01.052.

35. T. Cocker, D. Baillie, M. Buruma, et al., "Microscopic Origin of the Drude-Smith Model," *Physical Review B* 96, no. 20 (2017): 205439, https://doi.org/10.1103/PhysRevB.96.205439.

36. W. Chen and R. Marcus, "The Drude-Smith Equation and Related Equations for the Frequency-Dependent Electrical Conductivity of Materials: Insight From a Memory Function Formalism," *ChemPhysChem* 22, no. 16 (2021): 1667–1674, https://doi.org/10.1002/cphc.202100299.

37. F. Han, W. Xu, L. Li, and C. Zhang, "A Generalization of the Drude-Smith Formula for Magneto-Optical Conductivities in Faraday Geometry," *Journal of Applied Physics* 119, no. 24 (2016): 245706, https://doi.org/10.1063/1.4954889.

38. A. Iqbal, P. Sambyal, and C. Koo, "2D MXenes for Electromagnetic Shielding: A Review," *Advanced Functional Materials* 30, no. 47 (2020): 2000883, https://doi.org/10.1002/adfm.202000883.

39. H. L. Lv, Z. H. Yang, H. G. Pan, and R. B. Wu, "Electromagnetic Absorption Materials: Current Progress and New Frontiers," *Progress in Materials Science* 127 (2022): 100946, https://doi.org/10.1016/j.pmatsci.2022.100946.

40. B. Quan, X. Liang, G. Ji, et al., "Dielectric Polarization in Electromagnetic Wave Absorption: Review and Perspective," *Journal of Alloys and Compounds* 728 (2017): 1065–1075, https://doi.org/10.1016/j.jallcom.2017.09.082.

41. X. Meng, W. Lei, W. Yang, Y. Liu, and Y. Yu, "Fe_3O_4 Nanoparticles Coated With Ultra-Thin Carbon Layer for Polarization-Controlled Microwave Absorption Performance," *Journal of Colloid and Interface Science* 600 (2021): 382–389, https://doi.org/10.1016/j.jcis.2021.05.055.

42. L. Liang, W. Gu, Y. Wu, et al., "Heterointerface Engineering in Electromagnetic Absorbers: New Insights and Opportunities," *Advanced Materials* 34, no. 4 (2022): 2106195, https://doi.org/10.1002/adma.202106195.

43. P. Allen, "Theory of Thermal Relaxation of Electrons in Metals," *Physical Review Letters* 59, no. 13 (1987): 1460–1463, https://doi.org/10.1103/PhysRevLett.59.1460.

44. H. Lv, Y. Yao, S. Li, et al., "Staggered Circular Nanoporous Graphene Converts Electromagnetic Waves Into Electricity," *Nature*

Communications 14, no. 1 (2023): 1982, https://doi.org/10.1038/s41467-023-37436-6.

45. Z. Jin, D. Gehrig, C. Dyer-Smith, et al., "Ultrafast Terahertz Photoconductivity of Photovoltaic Polymer-Fullerene Blends: A Comparative Study Correlated With Photovoltaic Device Performance," *Journal of Physical Chemistry Letters* 5, no. 21 (2014): 3662–3668, https://doi.org/10.1021/jz501890n.

46. H. Yan, B. An, Z. Fan, et al., "Ultrafast Terahertz Probe of Photo-excited Free Charge Carriers in Organometal $CH_3NH_3PbI_3$ Perovskite Thin Film," *Applied Physics A* 122, no. 4 (2016): 414, https://doi.org/10.1007/s00339-016-9957-2.

47. Q. Zhou, Y. Shi, B. Jin, and C. Zhang, "Ultrafast Carrier Dynamics and Terahertz Conductivity of Photoexcited GaAs Under Electric Field," *Applied Physics Letters* 93, no. 10 (2008): 102103, https://doi.org/10.1063/1.2980026.

48. J. Baxter and G. Guglietta, "Terahertz Spectroscopy," *Analytical Chemistry* 83, no. 12 (2011): 4342–4368, https://doi.org/10.1021/ac200907z.

49. G. Chen, R. Zhang, M. Yuan, et al., "Visualizing Nanoscale Interlayer Magnetic Interactions and Unconventional Low-Frequency Behaviors in Ferromagnetic Multishelled Structures," *Advanced Materials* 36, no. 24 (2024): 2313411, https://doi.org/10.1002/adma.202313411.

50. A. Rahman, A. Ahmad, M. Helal, M. Hessien, G. Rahman, and S. Magalhaes, "Defect Induces Room Temperature Ferromagnetism and Half-Metallicity in Zr_2CO_2 MXene: Ab-Initio Calculations," *European Physical Journal Plus* 140, no. 1 (2025): 35, https://doi.org/10.1140/epjp/s13360-025-05975-0.

51. H. Tan, C. Wang, H. Duan, et al., "Intrinsic Room-Temperature Ferromagnetism in V_2C MXene Nanosheets," *ACS Applied Materials & Interfaces* 13, no. 28 (2021): 33363–33370, https://doi.org/10.1021/acsami.1c07906.

52. Y. Yue, "Fe_2C Monolayer: An Intrinsic Ferromagnetic MXene," *Journal of Magnetism and Magnetic Materials* 434 (2017): 164–168, https://doi.org/10.1016/j.jmmm.2017.03.058.

53. Y. Zhang and F. Li, "Robust Half-Metallic Ferromagnetism in Cr_3C_2 MXene," *Journal of Magnetism and Magnetic Materials* 433 (2017): 222–226, https://doi.org/10.1016/j.jmmm.2017.03.031.

54. H. Wang, X. Sun, S. Yang, et al., "3D Ultralight Hollow NiCo Compound@Mxene Composites for Tunable and High-Efficient Microwave Absorption," *Nano-Micro Letters* 13, no. 1 (2021): 206, https://doi.org/10.1007/s40820-021-00727-y.

55. S. Bonetti, M. Hoffmann, M. Sher, et al., "THz-Driven Ultrafast Spin-Lattice Scattering in Amorphous Metallic Ferromagnets," *Physical Review Letters* 117, no. 8 (2016): 087205, https://doi.org/10.1103/PhysRevLett.117.087205.

56. M. Yang, J. Tan, Z. Wang, et al., "Enhanced Electrical Conductivity by the Heavy Chalcogen Effect in Metal-Organic Frameworks," *Journal of the American Chemical Society* 147, no. 27 (2025): 24152–24161, https://doi.org/10.1021/jacs.5c08594.

57. T. Wang, E. Romanova, N. Abdel-Moneim, et al., "Time-Resolved Terahertz Spectroscopy of Charge Carrier Dynamics in the Chalcogenide Glass $As_{30}Se_{30}Te_{40}$," *Photonics Research* 4, no. 3 (2016): A22–A28, https://doi.org/10.1364/PRJ.4.000A22.

58. J. Buron, F. Pizzocchero, B. Jessen, et al., "Electrically Continuous Graphene From Single Crystal Copper Verified by Terahertz Conductance Spectroscopy and Micro Four-Point Probe," *Nano Letters* 14, no. 11 (2014): 6348–6355, https://doi.org/10.1021/nl5028167.

59. T. Magnanelli, S. Engmann, J. Wahlstrand, J. Stephenson, L. Richter, and E. Heilweil, "Polarization Dependence of Charge Conduction in Conjugated Polymer Films Investigated With Time-Resolved Terahertz Spectroscopy," *Journal of Physical Chemistry C* 124, no. 13 (2020): 6993–7006, https://doi.org/10.1021/acs.jpcc.9b11870.

60. S. Yang, Z. Lin, X. Wang, et al., "Stretchable, Transparent, and Ultra-Broadband Terahertz Shielding Thin Films Based on Wrinkled MXene Architectures," *Nano-Micro Letters* 16, no. 1 (2024): 165, https://doi.org/10.1007/s40820-024-01365-w.

61. P. Rasekh, A. Safari, M. Yildirim, et al., "Terahertz Nonlinear Spectroscopy of Water Vapor," *ACS Photonics* 8, no. 6 (2021): 1683–1688, https://doi.org/10.1021/acsphotonics.1c00056.

62. R. Damari, O. Weinberg, D. Krotkov, et al., "Strong Coupling of Collective Intermolecular Vibrations in Organic Materials at Terahertz Frequencies," *Nature Communications* 10, no. 1 (2019): 3248, https://doi.org/10.1038/s41467-019-11130-y.

63. L. Wu, M. Brahlek, R. Aguilar, et al., "A Sudden Collapse in the Transport Lifetime Across the Topological Phase Transition in $(Bi_{1-x}In_x)_2Se_3$," *Nature Physics* 9, no. 7 (2013): 410–414, https://doi.org/10.1038/nphys2647.

64. B. Cheng, T. Schumann, S. Stemmer, and N. Armitage, "Probing Charge Pumping and Relaxation of the Chiral Anomaly in a Dirac Semimetal," *Science Advances* 7, no. 16 (2021): eabg0914, https://doi.org/10.1126/sciadv.abg0914.

65. H. Chen, W. Padilla, J. Zide, A. Gossard, A. Taylor, and R. Averitt, "Active Terahertz Metamaterial Devices," *Nature* 444, no. 7119 (2006): 597–600, https://doi.org/10.1038/nature05343.

66. M. Ghidiu, M. Lukatskaya, M. Zhao, Y. Gogotsi, and M. Barsoum, "Conductive Two-Dimensional Titanium Carbide 'Clay' With High Volumetric Capacitance," *Nature* 516, no. 7529 (2014): 78–81, https://doi.org/10.1038/nature13970.

67. B. Fan, N. Li, B. Dai, et al., "Investigation of Adjacent Spacing Dependent Microwave Absorption Properties of Lamellar Structural $Ti_3C_2T_x$ MXenes," *Advanced Powder Technology* 31, no. 2 (2020): 808–815, https://doi.org/10.1016/j.apt.2019.11.035.

68. T. Yun, H. Kim, A. Iqbal, et al., "Electromagnetic Shielding of Monolayer MXene Assemblies," *Advanced Materials* 32, no. 9 (2020): 1906769, https://doi.org/10.1002/adma.201906769.

69. R. Rakhmanov, C. Shuck, J. Al Hourani, S. Ippolito, Y. Gogotsi, and G. Friedman, "Ultrathin MXene Film Interaction With Electromagnetic Radiation in the Microwave Range," *Applied Physics Letters* 123, no. 20 (2023): 204105, https://doi.org/10.1063/5.0176575.

70. A. Iqbal, J. Kwon, T. Hassan, et al., "Environmentally Stable and Highly Crystalline MXenes for Multispectral Electromagnetic Shielding up to Millimeter Waves, Advanced Functional Materials," *Advanced Functional Materials* 35, no. 18 (2025): 2409346, https://doi.org/10.1002/adfm.202409346.

71. N. Das, Y. Liu, K. Yang, W. Peng, S. Maiti, and H. Wang, "Single-Walled Carbon Nanotube/Poly(Methyl Methacrylate) Composites for Electromagnetic Interference Shielding," *Polymer Engineering & Science* 49, no. 8 (2009): 1627–1634, https://doi.org/10.1002/pen.21384.

72. N. Laman and D. Grischkowsky, "Terahertz Conductivity of Thin Metal Film," *Applied Physics Letters* 93, no. 5 (2008): 051105, https://doi.org/10.1063/1.2968308.

73. C. Cui, R. Guo, E. Ren, et al., "MXene-Based rGO/Nb_2CT_x/Fe_3O_4 Composite for High Absorption of Electromagnetic Wave," *Chemical Engineering Journal* 405 (2021): 126626, https://doi.org/10.1016/j.cej.2020.126626.

74. W. Feng, H. Luo, Y. Wang, et al., "Ti_3C_2 MXene: A Promising Microwave Absorbing Material," *RSC Advances* 8, no. 5 (2018): 2398–2403, https://doi.org/10.1039/C7RA12616F.

75. M. Han, X. Yin, H. Wu, et al., "Ti_3C_2 MXenes With Modified Surface for High-Performance Electromagnetic Absorption and Shielding in the X-Band," *ACS Applied Materials & Interfaces* 8, no. 32 (2016): 21011–21019, https://doi.org/10.1021/acsami.6b06455.

76. Y. Tong, M. He, Y. Zhou, et al., "Electromagnetic Wave Absorption Properties in the Centimetre-Band of $Ti_3C_2T_x$ MXenes With Diverse

Etching Time," *Journal of Materials Science: Materials in Electronics* 29, no. 10 (2018): 8078–8088, https://doi.org/10.1007/s10854-018-8814-9.

77. X. Chen, X. Wang, K. Wen, et al., "Electrically Aligned $Ti_3C_2T_x$ MXene Composite With Multilayered Gradient Structure for Broadband Microwave Absorption," *Carbon* 203 (2023): 706–716, https://doi.org/10.1016/j.carbon.2022.12.016.

78. M. Han, C. Shuck, A. Singh, et al., "Efficient Microwave Absorption With $V_{n+1}C_nT_x$ MXenes," *Cell Reports Physical Science* 3, no. 10 (2022): 101073, https://doi.org/10.1016/j.xcrp.2022.101073.

79. X. Zhou, J. Wen, Z. Wang, X. Ma, and H. Wu, "Broadband High-Performance Microwave Absorption of the Single-Layer $Ti_3C_2T_x$ MXene," *Journal of Materials Science & Technology* 115 (2022): 148–155, https://doi.org/10.1016/j.jmst.2021.11.029.

80. J. Zhang, N. Kong, S. Uzun, et al., "Scalable Manufacturing of Free-Standing, Strong $Ti_3C_2T_x$ MXene Films With Outstanding Conductivity," *Advanced Materials* 32, no. 23 (2020): 2001093, https://doi.org/10.1002/adma.202001093.

81. W. Luo, Y. Liu, C. Wang, et al., "Molten Salt Assisted Synthesis and Electromagnetic Wave Absorption Properties of $(V_{1-x-y}Ti_xCr_y)_2AlC$ Solid Solutions," *Journal of Materials Chemistry C* 9, no. 24 (2021): 7697–7705, https://doi.org/10.1039/D1TC01338F.

82. A. Cross and J. Simon, "Rotational Dynamics of a Solvated Dipole: A Molecular Dynamics Study of Dielectric Friction," *Journal of Chemical Physics* 86, no. 12 (1987): 7079–7083, https://doi.org/10.1063/1.452356.

83. L. Luo, I. Chatzakis, J. Wang, et al., "Broadband Terahertz Generation From Metamaterials," *Nature Communications* 5, no. 1 (2014): 3055, https://doi.org/10.1038/ncomms4055.

84. A. Gover and A. Yariv, "Free-Electron-Bound-Electron Resonant Interaction," *Physical Review Letters* 124, no. 6 (2020): 064801, https://doi.org/10.1103/PhysRevLett.124.064801.

85. J. Han, J. Park, M. Kim, et al., "Ultrahigh Conductive MXene Films for Broadband Electromagnetic Interference Shielding," *Advanced Materials* 37, no. 27 (2025): 2502443, https://doi.org/10.1002/adma.202502443.

86. Z. Zeng, M. Chen, Y. Pei, et al., "Ultralight and Flexible Polyurethane/Silver Nanowire Nanocomposites With Unidirectional Pores for Highly Effective Electromagnetic Shielding," *ACS Applied Materials & Interfaces* 9, no. 37 (2017): 32211–32219, https://doi.org/10.1021/acsami.7b07643.

87. D. Tao, C. Yang, C. Chen, et al., "Highly Flexible and Ultralight PVA-co-PE-AgNW/MXene Composite Film With Low Filling for Multistage Electromagnetic Interference Shielding," *Small* 21, no. 7 (2025): 2411752, https://doi.org/10.1002/smll.202411752.

88. L. Issman, M. Alper, S. Howard, et al., "Direct-Spun CNT Textiles for High-Performance Electromagnetic Interference Shielding in an Ultra-wide Bandwidth," *Carbon* 206 (2023): 166–180, https://doi.org/10.1016/j.carbon.2023.02.013.

89. D. Lai, X. Chen, and Y. Wang, "Controllable Fabrication of Elastomeric and Porous Graphene Films With Superior Foldable Behavior and Excellent Electromagnetic Interference Shielding Performance," *Carbon* 158 (2020): 728–737, https://doi.org/10.1016/j.carbon.2019.11.047.

90. L. Zhang, N. Alvarez, M. Zhang, et al., "Preparation and Characterization of Graphene Paper for Electromagnetic Interference Shielding," *Carbon* 82 (2015): 353–359, https://doi.org/10.1016/j.carbon.2014.10.080.

91. R. Song, B. Mao, Z. Wang, et al., "Comparison of Copper and Graphene-Assembled Films in 5G Wireless Communication and THz Electromagnetic-Interference Shielding," *Proceedings of the National Academy of Sciences of the United States of America* 17, no. 4 (2024): 3061–3067, https://doi.org/10.1007/s12274-023-6127-7.

92. G. Choi, F. Shahzad, Y. Bahk, et al., "Enhanced Terahertz Shielding of MXenes With Nano-Metamaterials," *Advanced Optical Materials* 6, no. 5 (2018): 1701076, https://doi.org/10.1002/adom.201701076.

93. T. Zhao, P. Xie, H. Wan, et al., "Ultrathin MXene Assemblies Approach the Intrinsic Absorption Limit in the 0.5–10 THz Band," *Nature Photonics* 17, no. 7 (2023): 622–628, https://doi.org/10.1038/s41566-023-01197-x.

94. H. Chen, A. Taylor, and N. Yu, "A Review of Metasurfaces: Physics and Applications," *Reports on Progress in Physics* 79, no. 7 (2016): 076401, https://doi.org/10.1088/0034-4885/79/7/076401.

95. P. Yu, L. Besteiro, Y. Huang, et al., "Broadband Metamaterial Absorbers," *Advanced Optical Materials* 7, no. 3 (2019): 1800995, https://doi.org/10.1002/adom.201800995.

96. K. Huo, S. Yang, J. Zong, J. Chu, Y. Wang, and M. Cao, "Carbon-Based EM Functional Materials and Multi-Band Microwave Devices: Current Progress and Perspectives," *Carbon* 213 (2023): 118193, https://doi.org/10.1016/j.carbon.2023.118193.

97. G. Li, K. Kushnir, Y. Dong, et al., "Equilibrium and Non-Equilibrium Free Carrier Dynamics in 2D $Ti_3C_2T_x$ MXenes: Thz Spectroscopy Study," *2D Materials* 5, no. 3 (2018): 035043, https://doi.org/10.1088/2053-1583/aacb9e.

98. G. Lui, V. Natu, T. Shi, M. Barsoum, and L. Titova, "Two-Dimensional MXenes $Mo_2Ti_2C_3T_z$ and $Mo_2TiC_2T_z$: Microscopic Conductivity and Dynamics of Photoexcited Carriers," *ACS Applied Energy Materials* 3, no. 2 (2020): 1530–1539, https://doi.org/10.1021/acsaem.9b01966.

99. Y. Guo, Z. Chen, Z. Jin, et al., "Dynamically Controllable Terahertz Electromagnetic Interference Shielding by Small Polaron Responses in Dirac Semimetal PdTe Thin Films," *Advanced Functional Materials* 34, no. 46 (2024): 2407749, https://doi.org/10.1002/adfm.202407749.

100. J. Ji, Y. Zhou, B. Zhou, et al., "Probing Carrier Dynamics in Large-Scale MBE-Grown $PtSe_2$ Films by Terahertz Spectroscopy," *ACS Applied Materials & Interfaces* 15, no. 44 (2023): 51319–51329, https://doi.org/10.1021/acsami.3c09792.

101. Y. Mou, Z. Wu, Y. Gao, Z. Yang, Q. Yang, and G. Zhang, "Determination of the Complex Refractivity of Au, Cu and Al in Terahertz and Far-Infrared Regions From Reflection Spectra Measurements," *Infrared Physics & Technology* 80 (2017): 58–64, https://doi.org/10.1016/j.carbon.2023.118193.

102. F. Hegmann, O. Ostroverkhova, and D. Cooke, "Probing Organic Semiconductors With Terahertz Pulses," *Photophysics of Molecular Materials* (2005): 367–428, https://doi.org/10.1002/3527607323.ch7.

103. P. Di Pietro, M. Ortolani, O. Limaj, et al., "Observation of Dirac Plasmons in a Topological Insulator," *Nature Nanotechnology* 8, no. 8 (2013): 556–560, https://doi.org/10.1038/nnano.2013.134.

104. T. Jeon and D. Grischkowsky, "Nature of Conduction in Doped Silicon," *Physical Review Letters* 78, no. 6 (1997): 1106–1109, https://doi.org/10.1103/PhysRevLett.78.1106.

105. N. Katzenellenbogen and D. Grischkowsky, "Electrical Characterization to 4 THz of N-Type and P-Type Gaas Using THz Time-Domain Spectroscopy," *Applied Physics Letters* 61, no. 7 (1992): 840–842, https://doi.org/10.1063/1.107762.

106. S. Chen, Q. Feng, W. Zhao, et al., "Direct Measurement of Terahertz Conductivity in a Gated Monolayer Semiconductor," *Nano Letters* 25, no. 19 (2025): 7998–8002, https://doi.org/10.1021/acs.nanolett.5c01605.

107. E. Li, J. Wei, T. Zhang, et al., "Charge Carriers Localization Effect Revealed Through Terahertz Spectroscopy of MXene: $Ti_3C_2T_x$," *Small* 20, no. 16 (2024): 2306200, https://doi.org/10.1002/smll.202306200.

108. M. Han, C. Shuck, R. Rakhmanov, et al., "Beyond $Ti_3C_2T_x$: Mxenes for Electromagnetic Interference Shielding," *ACS Nano* 14, no. 4 (2020): 5008–5016, https://doi.org/10.1021/acsnano.0c01312.

109. H. Kim and H. Alshareef, "MXetronics: Mxene-Enabled Electronic and Photonic Devices," *ACS Materials Letters* 2, no. 1 (2019): 55–70, https://doi.org/10.1021/acsmaterialslett.9b00419.

110. R. Li, W. Sun, C. Zhan, P. Kent, and D. Jiang, "Interfacial and Electronic Properties of Heterostructures of MXene and Graphene," *Physical Review B* 99, no. 8 (2019): 085429, https://doi.org/10.1103/PhysRevB.99.085429.

111. T. Wang, N. Li, Y. Li, J. Kai, and J. Fan, "M-Site Vacancy-Mediated Adsorption and Diffusion of Sodium on Ti_2CO_2 MXene," *Journal of Physical Chemistry C* 125, no. 1 (2020): 82–90, https://doi.org/10.1021/acs.jpcc.0c08302.

112. W. Luo, Y. Liu, C. Wang, et al., "Sacrificial Template Synthesis of $(V_{0.8}Ti_{0.1}Cr_{0.1})AlC$ and Carbon Fiber@$(V_{0.8}Ti_{0.1}Cr_{0.1})AlC_2$ Microrods for Efficient Microwave Absorption," *Journal of Materials Science & Technology* 111 (2022): 236–244, https://doi.org/10.1016/j.jmst.2021.10.018.

113. Y. Fei, Q. Wang, F. Wang, et al., "M-Site Dependent Terahertz Intrinsic Absorption in MXenes," *InfoMat* 7, no. 4 (2025): e12654, https://doi.org/10.1002/inf2.12654.

114. Y. He, D. Liu, Q. Su, B. Zhong, L. Xia, and X. Huang, "Cl-Terminated Decoration to Modulate the Permittivity of MXene for Enhanced Electromagnetic-Absorbing Performance," *Journal of Materials Science & Technology* 179 (2024): 187–197, https://doi.org/10.1016/j.jmst.2023.08.055.

115. M. Han, K. Maleski, C. Shuck, et al., "Tailoring Electronic and Optical Properties of MXenes Through Forming Solid Solutions," *Journal of the American Chemical Society* 142, no. 45 (2020): 19110–19118, https://doi.org/10.1021/jacs.0c07395.

116. T. Xu, J. Li, D. Zhao, X. Chen, G. Sun, and Z. Zhou, "Structural Engineering Enabled Bimetallic $(Ti_{1-y}Nb_y)_2AlC$ Solid Solution Structure for Efficient Electromagnetic Wave Absorption in Gigahertz," *Small* 19, no. 27 (2023): 2300119, https://doi.org/10.1002/smll.202300119.

117. G. Li, N. Amer, H. Hafez, et al., "Dynamical Control Over Terahertz Electromagnetic Interference Shielding With 2D $Ti_3C_2T_y$ MXene by Ultrafast Optical Pulses," *Nano Letters* 35, no. 1 (2022): 90–100, https://doi.org/10.1021/acs.nanolett.9b04404.

118. A. Lipatov, M. Alhabeb, M. Lukatskaya, A. Boson, Y. Gogotsi, and A. Sinitskii, "Effect of Synthesis on Quality, Electronic Properties and Environmental Stability of Individual Monolayer Ti_3C_2 MXene Flakes," *Advanced Electronic Materials* 2, no. 12 (2016): 1600255, https://doi.org/10.1002/aelm.201600255.

119. P. Michalowski, M. Anayee, T. Mathis, et al., "Oxycarbide MXenes and MAX Phases Identification Using Monoatomic Layer-by-Layer Analysis With Ultralow-Energy Secondary-Ion Mass Spectrometry," *Nature Nanotechnology* 17, no. 11 (2022): 1192–1197, https://doi.org/10.1038/s41565-022-01214-0.

120. A. Iqbal, F. Shahzad, K. Hantanasirisakul, et al., "Anomalous Absorption of Electromagnetic Waves by 2D Transition Metal Carbonitride Ti_3CNT_x (MXene)," *Science* 369, no. 6502 (2020): 446–450, https://doi.org/10.1126/science.aba7977.

121. I. Shein and A. Ivanovskii, "Graphene-Like Titanium Carbides and Nitrides $Ti_{n+1}C_n$, $Ti_{n+1}N_n$ (n =1, 2, and 3) From De-Intercalated MAX Phases: First-Principles Probing of Their Structural, Electronic Properties and Relative Stability," *Computational Materials Science* 65 (2012): 104–114, https://doi.org/10.1016/j.commatsci.2012.07.011.

122. T. Schultz, N. Frey, K. Hantanasirisakul, et al., "Surface Termination Dependent Work Function and Electronic Properties of $Ti_3C_2T_x$ MXene," *Chemistry of Materials* 31, no. 17 (2019): 6590–6597, https://doi.org/10.1021/acs.chemmater.9b00414.

123. S. Thomas and M. Zaeem, "Phosgene Gas Sensing of Ti_2CT_2 (T = F^-, O^-, OH^-) MXenes," *Advanced Theory and Simulations* 4, no. 3 (2021): 2000250, https://doi.org/10.1002/adts.202000250.

124. Y. Du, Z. Yan, W. You, et al., "Balancing MXene Surface Termination and Interlayer Spacing Enables Superior Microwave Absorption," *Advanced Functional Materials* 33, no. 34 (2023): 2301449, https://doi.org/10.1002/adfm.202301449.

125. D. Li, W. Zheng, S. Gali, et al., "MXenes With Ordered Triatomic-Layer Borate Polyanion Terminations," *Nature Materials* 23, no. 8 (2024): 1085–1092, https://doi.org/10.1038/s41563-024-01911-2.

126. M. Jiang, D. Wang, Y. Kim, C. Duan, D. Talapin, and C. Zhou, "Evolution of Surface Chemistry in Two-Dimensional MXenes: From Mixed to Tunable Uniform Terminations," *Angewandte Chemie-International Edition* 136, no. 37 (2024): e202409480, https://doi.org/10.1002/ange.202409480.

127. T. Zhang, L. Chang, X. Zhang, et al., "Simultaneously Tuning Interlayer Spacing and Termination of MXenes by Lewis-Basic Halides," *Nature Communications* 13, no. 1 (2022): 6731, https://doi.org/10.1038/s41467-022-34569-y.

128. C. Zhou, D. Wang, F. Lagunas, et al., "Hybrid Organic-Inorganic Two-Dimensional Metal Carbide MXenes With Amido- and Imido-Terminated Surfaces," *Nature Chemistry* 15, no. 12 (2023): 1722–1729, https://doi.org/10.1038/s41557-023-01288-w.

129. N. Liu, Q. Li, H. Wan, et al., "High-Temperature Stability in Air of $Ti_3C_2T_x$ MXene-Based Composite With Extracted Bentonite," *Nature Communications* 13, no. 1 (2022): 5551, https://doi.org/10.1038/s41467-022-33280-2.

130. R. Rakhmanov, S. Ippolito, M. Downes, et al., "Influence of MXene Interlayer Spacing on the Interaction With Microwave Radiation," *Advanced Functional Materials* 35, no. 18 (2025): 2410591, https://doi.org/10.1002/adfm.202410591.

131. Y. Shi, L. Chu, H. Wei, et al., "Modulation of Multifunctional Electric Dipoles on MXenes for Boosting Electromagnetic Interference Shielding," *Cell Reports Physical Science* 5, no. 4 (2024): 101903, https://doi.org/10.1016/j.xcrp.2024.101903.

132. R. Li, Y. Huangfu, L. Liu, et al., "Intercalation-Induced Interlayer and Defect Engineering in $Ti_3C_2T_x$ MXene for Ultralow-Reflection Electromagnetic Interference Shielding," *ACS Nano* 19, no. 2 (2025): 2777–2787, https://doi.org/10.1021/acsnano.4c15343.

133. W. Zheng, B. Sun, D. Li, et al., "Band Transport by Large Fröhlich Polarons in MXenes," *Nature Physics* 18, no. 5 (2022): 544–550, https://doi.org/10.1038/s41567-022-01541-y.

134. Q. Zhang, M. Levi, Y. Chai, et al., "Vacuum Filtration-and-Transfer Technique Helps Electrochemical Quartz Crystal Microbalance to Reveal Accurate Charge Storage in Supercapacitors," *Small Methods* 3, no. 11 (2019): 1900246, https://doi.org/10.1002/smtd.201900246.

135. B. Lyu, M. Kim, H. Jing, et al., "Large-Area MXene Electrode Array for Flexible Electronics," *ACS Nano* 13, no. 10 (2019): 11392–11400, https://doi.org/10.1021/acsnano.9b04731.

136. H. An, T. Habib, S. Shah, et al., "Surface-Agnostic Highly Stretchable and Bendable Conductive MXene Multilayers," *Science Advances* 4, no. 3 (2018): eaaq0118, https://doi.org/10.1126/sciadv.aaq0118.

137. Z. Wang, H. Kim, and H. Alshareef, "Oxide Thin-Film Electronics Using All-MXene Electrical Contacts," *Advanced Materials* 30, no. 15 (2018): 1706656, https://doi.org/10.1002/adma.201706656.

138. T. Guo, X. Xu, C. Liu, et al., "Large-Area Metal-Semiconductor Heterojunctions Realized via MXene-Induced Two-Dimensional Surface Polarization," *ACS Nano* 17, no. 9 (2023): 8324–8332, https://doi.org/10.1021/acsnano.2c12684.

139. Y. Shi, M. Osada, Y. Ebina, and T. Sasaki, "Single Droplet Assembly for Two-Dimensional Nanosheet Tiling," *ACS Nano* 14, no. 11 (2020): 15216–15226, https://doi.org/10.1021/acsnano.0c05434.

140. M. Mojtabavi, A. VahidMohammadi, K. Ganeshan, et al., "Wafer-Scale Lateral Self-Assembly of Mosaic $Ti_3C_2T_x$ MXene Monolayer

Films," *ACS Nano* 15, no. 1 (2021): 625–636, https://doi.org/10.1021/acsnano.0c06393.

141. K. Matsuba, C. Wang, K. Saruwatari, et al., "Neat Monolayer Tiling of Molecularly Thin Two-Dimensional Materials in 1 Min," *Science Advances* 3, no. 6 (2017): e1700414, https://doi.org/10.1126/sciadv.1700414.

142. T. Guo, D. Zhou, M. Gao, et al., "Large-Area Smooth Conductive Films Enabled by Scalable Slot-Die Coating of $Ti_3C_2T_x$ MXene Aqueous Inks," *Advanced Functional Materials* 33, no. 15 (2023): 2213183, https://doi.org/10.1002/adfm.202213183.

143. T. Guo, D. Zhou, S. Deng, et al., "Rational Design of $Ti_3C_2T_x$ MXene Inks for Conductive, Transparent Films," *ACS Nano* 17, no. 4 (2023): 3737–3749, https://doi.org/10.1021/acsnano.2c11180.

144. K. Sefiane, "Patterns From Drying Drops," *Advances in Colloid and Interface Science* 206 (2014): 372–381, https://doi.org/10.1016/j.cis.2013.05.002.

145. H. Kim, F. Boulogne, E. Um, I. Jacobi, E. Button, and H. Stone, "Controlled Uniform Coating From the Interplay of Marangoni Flows and Surface-Adsorbed Macromolecules," *Physical Review Letters* 116, no. 12 (2016): 124501, https://doi.org/10.1103/PhysRevLett.116.124501.

146. R. Deegan, O. Bakajin, T. Dupont, G. Huber, S. Nagel, and T. Witten, "Capillary Flow as the Cause of Ring Stains From Dried Liquid Drops," *Nature* 389, no. 6653 (1997): 827–829, https://doi.org/10.1038/39827.

147. Y. Shi, E. Yamamoto, M. Kobayashi, and M. Osada, "Automated One-Drop Assembly for Facile 2D Film Deposition," *ACS Applied Materials & Interfaces* 15, no. 18 (2023): 22737–22743, https://doi.org/10.1021/acsami.3c02250.

148. L. Cote, F. Kim, and J. Huang, "Langmuir-Blodgett Assembly of Graphite Oxide Single Layers," *Journal of the American Chemical Society* 131, no. 3 (2009): 1043–1049, https://doi.org/10.1021/ja806262m.

149. D. Wen, X. Zhou, Q. Fan, et al., "Ultrathin MXene Conductive Films With Percolation-Driven Electron Transport and Thickness-Dependent Microwave Absorption/Shielding Dual Functionality," *Nanoscale* 17, no. 29 (2025): 17040–17056, https://doi.org/10.1039/D5NR01970B.

150. S. Kim, J. Choi, K. Maleski, et al., "Interfacial Assembly of Ultrathin, Functional MXene Films," *ACS Applied Materials & Interfaces* 11, no. 35 (2019): 32320–32327, https://doi.org/10.1021/acsami.9b12539.

151. Y. Shi, H. Li, H. Tsunematsu, et al., "Ultrafast 2D Nanosheet Assembly via Spontaneous Spreading Phenomenon," *Small* 20, no. 36 (2024): 2403915, https://doi.org/10.1002/smll.202403915.

152. A. Dillon, M. Ghidiu, A. Krick, et al., "Highly Conductive Optical Quality Solution-Processed Films of 2D Titanium Carbide," *Advanced Functional Materials* 26, no. 23 (2016): 4162–4168, https://doi.org/10.1002/adfm.201600357.

153. S. Ahn, T. Han, K. Maleski, et al., "A 2D Titanium Carbide MXene Flexible Electrode for High-Efficiency Light-Emitting Diodes," *Advanced Materials* 32, no. 23 (2020): 2000919, https://doi.org/10.1002/adma.202000919.

154. N. Sakai and T. Sasaki, "Guidelines for Arranging 2D Nanosheets into Neatly Tiled Monolayer Films by a Spin-Coating Process," *Langmuir* 38, no. 40 (2022): 12399–12407, https://doi.org/10.1021/acs.langmuir.2c02211.

155. M. Li, T. Cheng, G. Liu, et al., "Infrared Anomalies in Ultrathin $Ti_3C_2T_x$ MXene Films," *arxiv preprint arxiv:2312.09573* (2023), https://doi.org/10.48550/arXiv.2312.09573.

156. C. Zhang, B. Anasori, A. Seral-Ascaso, et al., "Transparent, Flexible, and Conductive 2D Titanium Carbide (MXene) Films With High Volumetric Capacitance," *Advanced Materials* 29, no. 36 (2017): 1702678, https://doi.org/10.1002/adma.201702678.

157. Q. Li, Z. Tian, X. Zhang, et al., "Active Graphene-Silicon Hybrid Diode for Terahertz Waves," *Nature Communications* 6, no. 1 (2015): 7082, https://doi.org/10.1038/ncomms8082.

158. H. Lv, J. Cui, B. Li, M. Yuan, J. Liu, and R. Che, "Insights Into Civilian Electromagnetic Absorption Materials: Challenges and Innovative Solutions," *Advanced Functional Materials* 35, no. 18 (2025): 2315722, https://doi.org/10.1002/adfm.202315722.

159. H. Lv, Z. Yang, H. Xu, L. Wang, and R. Wu, "An Electrical Switch-Driven Flexible Electromagnetic Absorber," *Advanced Functional Materials* 30, no. 4 (2020): 1907251, https://doi.org/10.1002/adfm.201907251.

160. O. Balci, E. Polat, N. Kakenov, and C. Kocabas, "Graphene-Enabled Electrically Switchable Radar-Absorbing Surfaces," *Nature Communications* 6, no. 1 (2015): 6628, https://doi.org/10.1038/ncomms7628.

161. Y. Malevich, M. Ergoktas, G. Bakan, P. Steiner, and C. Kocabas, "Very-Large-Scale Reconfigurable Intelligent Surfaces for Dynamic Control of Terahertz and Millimeter Waves," *Nature Communications* 16, no. 1 (2025): 2907, https://doi.org/10.1038/s41467-025-58256-w.

162. S. Ummethala, T. Harter, K. Koehnle, et al., "THz-to-Optical Conversion in Wireless Communications Using an Ultra-Broadband Plasmonic Modulator," *Nature Photonics* 13, no. 8 (2019): 519–524, https://doi.org/10.1038/s41566-019-0475-6.

163. S. Yu, X. Wu, Y. Wang, X. Guo, and L. Tong, "2D Materials for Optical Modulation: Challenges and Opportunities," *Advanced Materials* 29, no. 14 (2017): 1606128, https://doi.org/10.1002/adma.201606128.

164. H. Lv, Z. Yang, P. Wang, et al., "A Voltage-Boosting Strategy Enabling a Low-Frequency, Flexible Electromagnetic Wave Absorption Device," *Advanced Materials* 30, no. 15 (2018): 1706343, https://doi.org/10.1002/adma.201706343.

165. X. Gan, C. Zhao, Y. Wang, et al., "Graphene-Assisted All-Fiber Phase Shifter and Switching," *Optica* 2, no. 5 (2015): 468–471, https://doi.org/10.1364/OPTICA.2.000468.

166. S. Gan, C. Cheng, Y. Zhan, et al., "A Highly Efficient Thermo-Optic Microring Modulator Assisted by Graphene," *Nanoscale* 7, no. 47 (2015): 20249–20255, https://doi.org/10.1039/C5NR05084G.

167. E. Piatti, A. Arbab, F. Galanti, et al., "Charge Transport Mechanisms in Inkjet-Printed Thin-Film Transistors Based on Two-Dimensional Materials," *Nature Electronics* 4, no. 12 (2021): 893–905, https://doi.org/10.1038/s41928-021-00684-9.

168. F. Yang, J. Yao, L. Jin, et al., "Multifunctional $Ti_3C_2T_x$ MXene/Aramid Nanofiber/Polyimide Aerogels With Efficient Thermal Insulation and Tunable Electromagnetic Wave Absorption Performance Under Thermal Environment," *Composites Part B: Engineering* 243 (2022): 110161, https://doi.org/10.1016/j.compositesb.2022.110161.

169. A. Lipatov, A. Goad, M. Loes, et al., "High Electrical Conductivity and Breakdown Current Density of Individual Monolayer $Ti_3C_2T_x$ MXene Flakes," *Matter* 4, no. 4 (2021): 1413–1427, https://doi.org/10.1016/j.matt.2021.01.021.

170. K. Hantanasirisakul, M. Alhabeb, A. Lipatov, et al., "Effects of Synthesis and Processing on Optoelectronic Properties of Titanium Carbonitride MXene," *Chemistry of Materials* 31, no. 8 (2019): 2941–2951, https://doi.org/10.1021/acs.chemmater.9b00401.

171. A. Lipatov, M. Alhabeb, H. Lu, et al., "Electrical and Elastic Properties of Individual Single-Layer $Nb_4C_3T_x$ MXene Flakes," *Advanced Electronic Materials* 6, no. 4 (2020): 1901382, https://doi.org/10.1002/aelm.201901382.

172. S. Bagheri, M. Loes, A. Lipatov, et al., "Synthesis of High-Quality Large $Cr_2TiC_2T_x$ MXene Monolayers, Their Mechanical Properties, P-type Electrical Transport, and Positive Photoresponse," *Matter* 7, no. 12 (2024): 4281–4296, https://doi.org/10.1016/j.matt.2024.08.019.

173. J. Zhang, R. Muñoz-Mármol, S. Fu, et al., "Interface-Tailored Secondary Excitation and Ultrafast Charge/Energy Transfer in

$Ti_3C_2T_x$-MoS_2 Heterostructure Films," *Journal of the American Chemical Society* 147, no. 11 (2025): 10012–10022, https://doi.org/10.1021/jacs.5c01826.

174. M. Liu, X. Yin, E. Ulin-Avila, et al., "A Graphene-Based Broadband Optical Modulator," *Nature* 474, no. 7349 (2011): 64–67, https://doi.org/10.1038/nature10067.

175. Y. Hu, M. Pantouvaki, J. Van Campenhout, et al., "Broadband 10 Gb/s Operation of Graphene Electro-Absorption Modulator on Silicon," *Laser & Photonics Reviews* 10, no. 2 (2016): 307–316, https://doi.org/10.1002/lpor.201500250.

176. B. Sensale-Rodriguez, R. Yan, M. Kelly, et al., "Broadband Graphene Terahertz Modulators Enabled by Intraband Transitions," *Nature Communications* 3, no. 1 (2012): 780, https://doi.org/10.1038/ncomms1787.

177. B. Sensale-Rodriguez, T. Fang, R. Yan, et al., "Unique Prospects for Graphene-Based Terahertz Modulators," *Applied Physics Letters* 99, no. 11 (2011): 113104, https://doi.org/10.1063/1.3636435.

178. H. Weng, A. Ranjbar, Y. Liang, et al., "Large-Gap Two-Dimensional Topological Insulator in Oxygen Functionalized MXene," *Physical Review B* 92, no. 7 (2015): 075436, https://doi.org/10.1103/PhysRevB.92.075436.

179. M. Khazaei, A. Ranjbar, M. Arai, and S. Yunoki, "Topological Insulators in the Ordered Double Transition Metals $M_2'M''C_2$ MXenes (M'= Mo, W; M''= Ti, Zr, Hf)," *Physical Review B.* 94, no. 12 (2016): 125152, https://doi.org/10.1103/PhysRevB.94.125152.

180. Y. Liang, M. Khazaei, A. Ranjbar, et al., "Theoretical Prediction of Two-Dimensional Functionalized MXene Nitrides as Topological Insulators," *Physical Review B* 96, no. 19 (2017): 195414, https://doi.org/10.1103/PhysRevB.96.195414.

181. Z. Huang, M. Xu, G. Macam, C. Hsu, and F. Chuang, "Large-Gap Topological Insulators in Functionalized Ordered Double Transition Metal Carbide MXenes," *Physical Review B* 102, no. 7 (2020): 075306, https://doi.org/10.1103/PhysRevB.102.075306.

182. A. Bafekry, C. Nguyen, C. Stampfl, B. Akgenc, and M. Ghergherehchi, "Oxygen Vacancies in the Single Layer of Ti_2CO_2 MXene: Effects of Gating Voltage, Mechanical Strain, and Atomic Impurities," *Physica Status Solidi (B)* 257, no. 12 (2020): 2000343, https://doi.org/10.1002/pssb.202000343.

183. G. Xing, H. Guo, X. Zhang, T. Sum, and C. Huan, "The Physics of Ultrafast Saturable Absorption in Graphene," *Optics Express* 18, no. 5 (2010): 4564–4573, https://doi.org/10.1364/OE.18.004564.

184. Q. Zhang, J. Li, J. Wen, et al., "Simultaneous Capturing Phonon and Electron Dynamics in MXenes," *Nature Communications* 13, no. 1 (2022): 7900, https://doi.org/10.1038/s41467-022-35605-7.

185. Z. Tong, S. Li, X. Ruan, and H. Bao, "Comprehensive first-principles Analysis of Phonon Thermal Conductivity and Electron-Phonon Coupling in Different Metals," *Physical Review B* 100, no. 14 (2019): 144306, https://doi.org/10.1103/PhysRevB.100.144306.

186. Y. Huang, J. Zhou, G. Wang, and Z. Sun, "Abnormally Strong Electron-Phonon Scattering Induced Unprecedented Reduction in Lattice Thermal Conductivity of Two-Dimensional Nb_2C," *Journal of the American Chemical Society* 141, no. 21 (2019): 8503–8508, https://doi.org/10.1021/jacs.9b01742.

187. J. Tang, H. Wan, L. Chang, et al., "Tunable Infrared Sensing Properties of MXenes Enabled by Intercalants," *Advanced Optical Materials* 10, no. 17 (2022): 2200623, https://doi.org/10.1002/adom.202200623.

188. M. Han, D. Zhang, C. Shuck, et al., "Electrochemically Modulated Interaction of MXenes With Microwaves," *Nature Nanotechnology* 18, no. 4 (2023): 373–379, https://doi.org/10.1038/s41565-022-01308-9.

189. W. Fei, J. Li, L. Ma, et al., "Electrochemically-Switched Microwave Response of MXene in Organic Electrolyte," *Advanced Materials* 36, no. 52 (2024): 2413311, https://doi.org/10.1002/adma.202413311.

190. I. Gutiérrez-Lezama, N. Ubrig, E. Ponomarev, and A. Morpurgo, "Ionic Gate Spectroscopy of 2D Semiconductors," *Nature Reviews Physics* 3, no. 7 (2021): 508–519, https://doi.org/10.1038/s42254-021-00317-2.

191. Y. Wu, D. Li, C. Wu, H. Hwang, and Y. Cui, "Electrostatic Gating and Intercalation in 2D Materials," *Nature Reviews Materials* 8, no. 1 (2023): 41–53, https://doi.org/10.1038/s41578-022-00473-6.

192. O. Zheliuk, J. Lu, Q. Chen, A. El Yumin, S. Golightly, and J. Ye, "Josephson Coupled Ising Pairing Induced in Suspended MoS_2 Bilayers by Double-Side Ionic Gating," *Nature Nanotechnology* 14, no. 12 (2019): 1123–1128, https://doi.org/10.1038/s41565-019-0564-1.

193. R. Maniyara, D. Rodrigo, R. Yu, et al., "Tunable Plasmons in Ultrathin Metal Films," *Nature Photonics* 13, no. 5 (2019): 328–333, https://doi.org/10.1038/s41566-019-0366-x.

194. J. Grenier, A. Wattiaux, J. Doumerc, et al., "Electrochemical Oxygen Intercalation Into Oxide Networks," *Journal of Solid State Chemistry* 96, no. 1 (1992): 20–30, https://doi.org/10.1016/S0022-4596(05)80293-2.

195. C. Hartwigsen, W. Witschel, and E. Spohr, "Charge Density and Charge Transfer in Stage-1 Alkali-Graphite Intercalation Compounds," *Physical Review B* 55, no. 8 (1997): 4953–4959, https://doi.org/10.1103/PhysRevB.55.4953.

196. S. Fleischmann, Y. Zhang, X. Wang, et al., "Continuous Transition From Double-Layer to Faradaic Charge Storage in Confined Electrolytes," *Nature Energy* 7, no. 3 (2022): 222–228, https://doi.org/10.1038/s41560-022-00993-z.

197. X. Wang, S. Bak, M. Han, et al., "Surface Redox Pseudocapacitance of Partially Oxidized Titanium Carbide MXene in Water-in-Salt Electrolyte," *ACS Energy Letters* 7, no. 1 (2021): 30–35, https://doi.org/10.1021/acsenergylett.1c02262.

198. P. Simon and Y. Gogotsi, "Perspectives for Electrochemical Capacitors and Related Devices," *Nature Materials* 19, no. 11 (2020): 1151–1163, https://doi.org/10.1038/s41563-020-0747-z.

199. S. Yu, X. Wu, K. Chen, et al., "All-Optical Graphene Modulator Based on Optical Kerr Phase Shift," *Optica* 3, no. 5 (2016): 541–544, https://doi.org/10.1364/OPTICA.3.000541.

200. S. Yu, C. Meng, B. Chen, et al., "Graphene Decorated Microfiber for Ultrafast Optical Modulation," *Optics Express* 23, no. 8 (2015): 10764–10770, https://doi.org/10.1364/OE.23.010764.

201. F. Zhou and W. Du, "Ultrafast All-Optical Plasmonic Graphene Modulator," *Applied Optics* 57, no. 23 (2018): 6645–6650, https://doi.org/10.1364/AO.57.006645.

202. R. Li, X. Ma, J. Li, et al., "Flexible and High-Performance Electrochromic Devices Enabled by Self-Assembled 2D TiO_2/MXene Heterostructures," *Nature Communications* 12, no. 1 (2021): 1587, https://doi.org/10.1038/s41467-021-21852-7.

203. S. Li, J. Li, Y. Wang, et al., "Large Transport Gap Modulation in Graphene via Electric-Field-Controlled Reversible Hydrogenation," *Nature Electronics* 4, no. 4 (2021): 254–260, https://doi.org/10.1038/s41928-021-00548-2.

204. M. Nikoo and E. Matioli, "Electronic Metadevices for Terahertz Applications," *Nature* 614, no. 7948 (2023): 451–455, https://doi.org/10.1038/s41586-022-05595-z.

205. C. Wu, H. Yuan, Y. Li, Y. Gong, H. Hwang, and Y. Cui, "Gate-Induced Metal-Insulator Transition in MoS_2 by Solid Superionic

Conductor LaF_3," *Nano Letters* 18, no. 4 (2018): 2387–2392, https://doi.org/10.1021/acs.nanolett.7b05377.

206. J. Pu, Y. Yomogida, K. Liu, L. Li, Y. Iwasa, and T. Takenobu, "Highly Flexible MoS_2 Thin-Film Transistors With Ion Gel Dielectrics," *Nano Letters* 12, no. 8 (2012): 4013–4017, https://doi.org/10.1021/nl301335q.

207. T. Li, T. Tu, Y. Sun, et al., "A Native Oxide High-κ Gate Dielectric for Two-Dimensional Electronics," *Nature Electronics* 3, no. 8 (2020): 473–478, https://doi.org/10.1038/s41928-020-0444-6.

208. Z. Lu, Y. Chen, W. Dang, et al., "Wafer-Scale High-κ Dielectrics for Two-Dimensional Circuits via van der Waals Integration," *Nature Communications* 14, no. 1 (2023): 2340, https://doi.org/10.1038/s41467-023-37887-x.

209. Y. Wu, C. La-o-Vorakiat, X. Qiu, et al., "Graphene Terahertz Modulators by Ionic Liquid Gating," *Advanced Materials* 27, no. 11 (2015): 1874–1879, https://doi.org/10.1002/adma.201405251.

210. B. Sensale-Rodriguez, R. Yan, S. Rafique, et al., "Extraordinary Control of Terahertz Beam Reflectance in Graphene Electro-Absorption Modulators," *Nano Letters* 12, no. 9 (2012): 4518–4522, https://doi.org/10.1021/nl3016329.